Structural, Ordering and Magnetic Properties of PtNi Nanoalloys Explored by Density Functional Theory and Stability Descriptors

Juan Esteban Montoya Cardona, Antoine Salichon, Nathalie Tarrat, Emilie Gaudry, David Loffreda

Structural, Ordering and Magnetic Properties of PtNi Nanoalloys Explored by Density Functional Theory and Stability Descriptors

Juan Esteban Montoya Cardona,[†,‡] Antoine Salichon,[¶] Nathalie Tarrat,[§] Emilie Gaudry,[*,†] and David Loffreda[*,¶]

†*Université de Lorraine, CNRS, Institut Jean Lamour UMR 7198, Campus Artem, 2 Allée André Guinier, 54011 Nancy Cedex, France*

‡*Université de Lorraine, Mines Nancy, Campus Artem, 2 Allée André Guinier, 54011 Nancy Cedex, France*

¶*ENSL, CNRS, Laboratoire de Chimie UMR 5182, 46 Allée d'Italie, 69364 Lyon Cedex, France*

§*CEMES, CNRS, Université de Toulouse, 29 Rue Jeanne Marvig, 31055 Toulouse, France*

E-mail: emilie.gaudry@univ-lorraine.fr; david.loffreda@ens-lyon.fr

Phone: +33(0)472448843

Abstract

Monometallic platinum and nickel nanoparticles, and platinum-nickel nanoalloys are examined in the range 13-976 atoms from density functional theory calculations. A large set of competitive symmetries and morphologies are considered including the usual Mackay icosahedral, Marks-decahedral and truncated octahedral forms. A comparative analysis of relative stability order is addressed on the basis of four stability descriptors all predicted at the *ab initio* level from spin-polarized calculations including van der Waals interactions. For platinum nanoparticles, they unanimously conclude on the preference of truncated octahedral morphology in the range 147-201 atoms. For nickel and platinum-nickel nanoclusters, three descriptors (cohesion energy, nanoparticle surface energy and vibrational band center) also support such octahedral symmetry (with a skin-heart chemical ordering for nanoalloys), whereas the excess energy rather favors the icosahedral morphology (with multishell and core-shell arrangement). Such discrepancies feed the debate related to the impact of the normalization on the predictive power of these descriptors and recall the high importance of validating theoretical models from a quantitative standpoint. This work invites the experimentalists to synthesize, characterize and measure surface energetics of PtNi nanolloys in highly controlled operating conditions.

Introduction

PtNi catalysts were proposed in the literature twenty years ago as efficient electrocatalysts for the oxygen reduction reaction (ORR) in the context of polymer electrolyte membrane fuel cells (PEMFCs) and applications in the automotive industry. The role of the second metal nickel is to ensure good catalytic properties for the corresponding alloy with respect to the reference pure platinum catalyst, while decreasing the whole amount of Pt. This helps reducing the cost, which hinders the commercialization of these catalysts.[1,2] There exist several platinum-based heterogeneous electrocatalyst approaches.[3] In the first stud-

ies, polycrystalline Pt_3Ni alloy was investigated by low energy ion scattering spectroscopy (LEISS) to establish the surface compositions. These measurements showed the generation of a "Pt-skin" at the surface of the electrocatalyst corresponding to a pure platinum termination. Such a platinum segregation at the surface makes these Ni-rich systems particularly stable and resistant to leaching in the electrolyte (responsible for deactivation).[4] Apart from the reduction of the catalyst cost, the presence of Ni as a second metal also improves the catalytic performance, by a factor 4 according to first experimental studies, thus making PtNi catalysts cost-efficient for ORR.[2] Moreover, the tailored $Pt_3Ni(111)$ surface is 10 times more active for the ORR than the corresponding Pt(111) surface and 90 times more efficient than the current state-of-the-art Pt/C catalysts for PEMFCs.[5]

Thanks to the remarkable performance observed for extended surfaces of $Pt_3Ni(111)$, many experimental studies have been devoted to the synthesis and catalytic tests of PtNi/C electro-nanocatalysts for ORR. To mimic the high specific activity of $Pt_3Ni(111)$ extended surfaces, Pt_3Ni octahedral nanoparticles have been synthesized and have also exhibited a larger performance than reference Pt and Pt_3Ni nanocubes.[6] Regarding chemical composition, the highest specific activity is observed for the 1:1 PtNi stoichiometry, while Pt_3Ni and $PtNi_3$ exhibit lower but similar performances. Although octahedral PtNi/C nanocatalysts are interesting from the standpoint of their activity toward ORR, their surface structures are of "Pt-skeleton" type, i.e., with many surface defects and deep cavities (often resulting from Ni leaching). This means that those nanoparticles do not present a similar high stability as the one of Pt-skin terminated extended $Pt_3Ni(111)$ surfaces. In addition, Pt-skeleton terminated catalysts have been found to be less active than Pt-skin terminated ones.[7]

Although $Pt_3Ni(111)$ surfaces exhibit a much larger catalytic performance toward ORR than other pure Pt reference catalysts, their high cost due the high precious metal content prevents their use in the mass production of fuel cells. A promising approach aiming to drastically decrease the precious metal content in the catalyst, while keeping enough active sites, is the synthesis of hollow and porous bimetallic nanoparticles which offer a signif-

icantly enhanced area-to-volume ratio.[8] In this context, Chen *et al.* have synthesized a highly active and durable class of Pt-Ni electrocatalysts by exploiting the structural evolution of these bimetallic nanocrystals.[9] The generated catalytic systems of diameter 15 nm are called Pt_3Ni nanoframes and they achieved a factor of 36 enhancement in mass activity and a factor of 22 enhancement in specific activity toward the ORR, compared to state-of-the-art Pt/C reference catalysts, during prolonged exposure to reaction conditions. The elegance of this synthesis stems from the relatively simple procedure and the precise thermal control over the resulting material, making this process amenable to scaling up for production. These cost-efficient Pt_3Ni hollow nanoframes contain 85% less precious metal with respect to equivalent size nanoalloys, while maintaining remarkable durability over 10000 electrocatalytic cycles. Thanks to an open architecture and the successful formation of a Pt-skin surface, these catalytic bimetallic materials provide an easy access of the reactants to the active sites and maximize the specific activity.[10–12] According to these studies and for chemical compositions in the range $Pt_{80}Ni_{20}$-$Pt_{88}Ni_{12}$, the presence of defects such as excavation of the facets of the nanocatalysts (concave facets) is an important property for providing good catalytic performance toward ORR.[11,13,14] However, only the surface segregation of platinum leading to the so-called Pt-skin termination allows optimal catalytic performance.[10,11] Dendrite-embedded Pt-Ni multiframes have also been synthesized and have shown a higher performance toward ORR by comparison with state-of-the-art Pt/C catalyst.[15] Such performance has been attributed to the porous nanostructure and numerous active sites exposed on surface grain boundaries and high-indexed facets.

Conventional polyhedrons (e.g., cubes, octahedrons, and tetrahedrons) and their overgrown structures (e.g., multipods) have all been obtained in reasonably high yields, as well as some unconventional shapes (e.g., tetrahexahedrons). Compared to commercially available Pt catalysts, these well-defined nanocrystals exhibit greatly enhanced activity and selectivity for a range of reactions.[16] For instance, the exploration of the synthesis and the catalytic performance of PtNi nanocrystals have been reported in the literature. PtNi nanocrystals

smaller than 10 nm and composed of an octahedral structure with a Pt core and a Pt-Ni outer-shell have exhibited a particular stability over ORR cycling.[17] A similar interesting performance has been registered for much larger Pt-Ni core-shell nanoparticles.[18,19] Among other morphologies, PtNi nanowires have also been synthesized and tested for the ORR, showing lower performance and durability with respect to other working principles.[20,21] Before these studies, PtNi alloy nanowires transformed into jagged Pt nanowires via subsequent thermal annealing process and electrochemical dealloying had yielded an interesting mass activity.[22] PtNi hexapods have been synthesized and compared to other polyhedrons and nanoparticles regarding their catalytic performance toward ORR and they have shown a superior mass activity.[23] More recently, PtNi nanoparticles and single (Pt, Ni) atom catalysts supported on nitrogen-doped carbon and graphene have also been synthesized and compared with reference systems with promising perspectives.[24–26]

In summary, over the last two decades, many experimental efforts have been devoted to the exploration of the catalytic performance of PtNi electrocatalysts toward ORR. Interestingly, a binary experimental descriptor capturing the strain and the Pt transition metal coupling contributions through X-ray absorption spectroscopy has been introduced recently to validate experimentally a Sabatier plot aiming to predict catalytic activity and stability for a wide range of Pt-alloy ORR catalysts. Such an approach has led to the design of highly active and stable slow-dealloyed PtNiCo materials.[27] However little is known regarding the origin of the measured performance and especially about the nature of the active sites. An interesting alternative approach to determine at the atomic scale the catalytic properties of these nanoparticles is the theoretical modeling. For single crystal surfaces and the prediction of corresponding catalytic measurements, Density Functional Theory (DFT) models of $Pt_3Ni(111)$ surfaces have successfully explained the kinetic origin of the superior activity for Pt-skin alloy termination compared to Pt-skeleton, bulk truncated alloy terminations and Pt(111) reference toward ORR.[28,29] Over the last 30 years, several theoretical approaches have been developed to explore the morphology and related stability of monometallic Pt and

Ni, and alloy PtNi nanoclusters. Depending on the size of these clusters, the accuracy level regarding the energetics of these approaches has varied from classical force fields and semi-empirical or effective potentials to *ab initio* methods including Wavefunction Theory (WFT) and DFT. Small monometallic Pt and Ni clusters (1-147 atoms) have been studied by a wide range of theoretical tools, including global optimization methods and Monte-Carlo simulations.[30–40] The competition between classical symmetries such as octahedral, decahedral and icosahedral is often explored in these studies, as well as non-symmetric and amorphous clusters. For pure Pt clusters at the size 1.7 nm, the face-centered-cubic (FCC) packing and truncated octahedral structure have been proposed as the most stable form from Embedded Atom Model (EAM) and DFT calculations by comparison with X-ray diffraction measurements.[37] For much larger pure Pt clusters (up to 40000 atoms), the decahedral shape is preferential in the range 100-6500 atoms, while the truncated octahedral structure is favored above 6500 atoms, according to EAM or Rosato, Guillopé and Legrand (RGL) effective potentials and global optimization methods.[41,42] These results are in partial agreement with another Equivalent Crystal Theory, a Quantum Approximate Method, (ECT/QAM) study, showing a crossover between $D5h$ and Oh forms at 3300 atoms.[43,44] According to a recent study based on symmetry-constrained genetic algorithm and neural network potential (SCGA-NNP) trained by DFT calculations with the revised PBE functional, other conclusions have been drawn in favor of the truncated octahedra which appear as the most stable Pt clusters over the explored range of sizes (1.5-5 nm).[40] For usual magic numbers of pure Ni clusters up to 5083 atoms, the Mackay icosahedral structure is found to be more stable than the cuboctahedral shape from EAM-based simulations.[31] These results agree with a very early study also concluding on a preference of the icosahedral shape up to 2300 atoms.[45] Another more recent study based on EAM and RGL potentials has reported on partially different conclusions.[42] According to these works, the icosahedral form is the most stable one in the range 1-1200 atoms, whereas the decahedral shape becomes preferential in the range 1200-60000 atoms (the truncated octahedral clusters being the most stable ones above

60000 atoms). Another ECT/QAM study has also shown the predominance of decahedral clusters but in a different range 2300-30000 atoms (icosahedra being more stable below 2300 atoms and octahedra above 30000 atoms).[43] A recent SCGA-NNP study also concludes on a very early crossing between icosahedral and truncated octahedral Ni clusters; the latter becoming more stable above 1.75 nm.[40]

Regarding the theoretical models of PtNi nanoparticles, a few studies have reported on specific morphologies and composition,[4,46–52] while a more complete SCGA-NNP investigation has been addressed recently in the range 140-4033 atoms (1.5-5 nm).[40] In the small size range (38-55 atoms), heuristic approaches based on a spin-polarized DFT methodology[49] were developed as well as global optimization methods based on Gupta potential.[52] At the size of 55 atoms, DFT calculations have predicted a preference for a core-shell icosahedral structure with a core of Ni and an outer-shell of Pt with strong magnetic properties evolving with the chemical composition (the ferromagnetism being increased in the nanoparticle with respect to the corresponding bulk system).[49] From Gupta potential and global optimization methods, a *FCC* structure is found more stable for the $Pt_{28}Ni_{27}$ cluster over the icosahedral symmetry.[52] This example shows the reported discrepancies regarding the conclusions for a particular PtNi cluster of 55 atoms. At the size of 38 atoms for $Pt_{20}Ni_{18}$, sixfold pancake polyicosahedra have been found this time to be more stable than truncated octahedra according to the same authors.[52] For larger PtNi nanoparticles (201-923 atoms), only the octahedral symmetry has been examined by effective potentials (such as Modified EAM or second-moment approximation of the tight-binding potential) or force fields (ReaxFF) and basin hopping-based global optimization methods, Grand Canonical Monte Carlo and classical Molecular Dynamics simulations.[4,46,48,50,51] For nanoclusters of respectively 586 atoms[46,51] and 670 atoms[4] and a chemical composition of $Pt_{75}Ni_{25}$, a multishell arrangement is obtained in both studies thanks to a segregation of Pt from the second layer to the surface layer leading to an almost complete Pt-skin outer-shell. Such a strong Pt surface segregation accompanied by a Ni segregation to the subsurface has also been registered systematically

from a SCGA-NNP recent work.[40] Icosahedral PtNi nanoclusters are found predominant at 1:1 composition for almost all considered sizes with the formation of flower-like ordering pattern. Truncated octahedral PtNi nanoparticles become more competitive in the Pt-rich and Ni-rich composition domains, with the presence of PtNi ordered phases in their interiors. These results are also confirmed by the theoretical study of PtNi nanowires.[47] For the truncated octahedral cluster of 586 atoms, a Ni-enrichment in the second layer has been seen in agreement with measurements on the $Pt_3Ni(111)$ surface.[46] In the case of the *FCC* clusters of 670 atoms, the octahedral shape has been found to be preferential over the tetrahedral form.[4] Cuboctahedral structures have also been examined at the sizes 561 and 923 atoms with the same classical approaches. They have exhibited two ordered phases of $L1_2$ ($PtNi_3$) and $L1_0$ (PtNi) consistently with the experimental phase diagram of the PtNi bulk alloy.[48] Surface reconstructions in pyritohedral forms have also been reported on Ni@Pt core@shell (Pt-skin) clusters of regular truncated octahedral (201 and 586 atoms) and on non-regular truncated octahedral (260, 405 and 459 atoms) shapes, showing again the morphological versatility of such complex nanoalloys.[50]

At the theoretical level, another source of difficulty comes from the choice of the theoretical descriptor capturing the stability of the clusters and related competitive morphologies. From the historical point of view, Miedema's model[53,54] based on energetic measurements of solid metals and further developments related to collision-induced dissociation of Ni clusters[55] had introduced the cohesion energy of monometallics normalized to the total number of atoms (N) as an interesting descriptor to capture linear trends against $N^{-1/3}$. A DFT investigation of small Ni clusters could have reproduced such a linear trend at the qualitative level without predicting the cohesion energy accurately compared to measurements.[30,31,33,55] An alternative interesting descriptor named the excess energy (referenced to the bulk system instead of the isolated atom) has been introduced in the nineties,[45] with a different normalization corresponding to $N^{2/3}$, introduced as an approximation of the number of surface atoms.[41–43] Unfortunately, such a descriptor, which is not an observable, could not have

been validated quantitatively with a direct comparison with measurements. Among the alternatives, the nanoparticle surface energy defined as an excess energy referenced to the nanoparticle surface area has also been widely studied in the theoretical literature from various approaches based on thermodynamics considerations and DFT calculations.[56–62] This descriptor can be measured for nanoparticles[63,64] and a recent experimental study has shown its relevance for capturing the nanoparticle stability of liquid Au, Cu and AuCu nanoalloys.[64]

In summary, the theoretical predictions of energetic, composition and structural properties of monometallic Pt and Ni nanoparticles, and PtNi nanoalloys in vacuum is a timely challenge. Although significant efforts have been conceded over the years to explore the morphological competition for pure nanoclusters and restricted families of PtNi nanoalloys, only a few theoretical studies have been based on DFT calculations at the generalized gradient approximation (GGA) level and only for small cluster size, up to date. A systematic comparison of several alternative stability descriptors for a complete set of large size high symmetry Pt, Ni and PtNi clusters based on spin-polarized DFT calculations, with the consideration of long-range van der Waals interactions, is not available yet.

In this work, we expose Density Functional Theory calculations for a large set of structures of monometallic Pt, Ni and bimetallic PtNi nanoparticles in the range 13-976 atoms. Spin polarization is systematically included in the predictions of Ni-containing nanoclusters, whereas van der Waals interactions are considered for all systems. The usual high symmetries and convex morphologies in competition have been compared including Mackay icosahedral form and defective structures presenting concavities such as Marks-decahedral shapes. For bimetallic PtNi nanoparticles, the chemical ordering (composition and arrangement) has been explored by a Heuristic approach with a finite set including crystalline and regular alloyed clusters and non-crystalline core-shell, multishell and skin-heart structures. Several stability descriptors usually considered in the literature have been computed and analyzed comparatively with a new one named vibrational band center which is introduced in this study.

Methodology

Dispersion-corrected DFT calculations have been performed by using the VASP code (version 5.4.4 and 6.2)[65–68] together with the density-dependent energy correction dDsC[69,70] combined with PBE functional[71] which has been chosen as a reasonable compromise to predict simultaneously bulk structural properties (for Pt, Ni, Pt_3Ni and $PtNi_3$ FCC bulks), cohesion energies, surface energies and magnetic properties with weak van der Waals forces (see Tables S1-S3 of the Supporting Information for the justification of this choice). The interactions between electrons and ion cores have been described by potentials generated by the Projector Augmented-Wave method (10 valence electrons per Pt and Ni atom).[72] Valence electrons have been described with plane wave basis sets in standard conditions (with a kinetic energy cutoff of 270 eV). A large simulation box (50×50×50 $Å^3$) has been used in order to ensure a minimum vacuum space of 1.8 nm between periodically equivalent nanoparticles. For the nanoparticle (NP) models, the Brillouin zone sampling in reciprocal space corresponds to the Γ point. For dealing with the partial occupancies, a Methfessel–Paxton smearing was used with a default value of 0.2 eV. The geometry of all the nanoalloys has been completely relaxed, with a tight convergence criterion of 10^{-6} eV for the total electronic energy, until all residual forces on nuclei are lower than ±0.01 eV.$Å^{-1}$. For the pure Pt and Ni bulk references, the grid of the Brillouin zone used for determining the total electronic energy was 43×43×43 k-points for the primitive rhombohedral cell containing one metallic atom (useful for GGA PBE, PBE-D3(0D) and optB86b-vdW functionals) and 31×31×31 k-points for the equivalent smallest centered cubic supercell composed of 4 atoms (required for PBE+dDsC functional). For the alloyed PtNi bulk references, the used mesh is 31×31×31 k-points for all the primitive centered cubic supercells for all the considered functionals.

Spin polarization has been systematically considered for the nanoparticles containing Ni (monometallic Ni clusters and PtNi nanoalloys). According to our DFT results, a global trend in favor of a ferromagnetic state ordering has been predicted with the spin held by Ni atoms, in agreement with measurements for Ni bulk (0.6 μ_B, see Table S1) and for Ni and

PtNi NPs, which are ferromagnetic.[34,49,73] The total spin polarizations have been reported either in Table 1 for pure Ni and PtNi NPs in the range 147-201 atoms or in Tables S4-S8 of the SI for all the other nanoclusters. Note in passing that the convergence of total electronic energy and spin polarization is not straightforward from standard computational conditions, for large size pure Ni and bimetallic PtNi nanoparticles (especially in the range 561-976 atoms). This comes from the magneto-structural correlation which requires a particular care for the initial structural guesses of the geometry optimizations. The calculation of harmonic vibrations of the nanoclusters has been performed by the finite difference approach on the basis of small variations of forces around the equilibrium structures. All the degrees of freedom of Pt and Ni atoms have been included in the calculations. The harmonic frequencies and related normal modes have been evaluated by diagonalizing the Hessian matrix determined with an atomic displacement of 0.03 Å and similar computational conditions as geometry optimizations. Spin polarization has been considered in all the vibration calculations.

Concerning the stability of the nanoparticles, several descriptors have been selected and compared. The first descriptor is the excess energy of the nanocluster ($E_{exc}(N_{\rm Ni}, N_{\rm Pt})$) computed as the difference between the total cohesion energy in the nanocluster ($E_{coh}^{NP}(N_{\rm Ni}, N_{\rm Pt})$) composed of $N_{\rm Pt}$ Pt atoms and $N_{\rm Ni}$ Ni atoms, and the total cohesion energy of the Pt bulk ($E_{coh}^{\text{bulk Pt}}$) and of the Ni bulk ($E_{coh}^{\text{bulk Ni}}$). This excess energy is normalized by $(N_{\rm Ni} + N_{\rm Pt})^{\frac{2}{3}}$, defined as an approximation of the total number of surface atoms of the nanoparticle, and this corresponds to a historical descriptor to evaluate the stability order of nanoparticles in global optimization methods.[41,42]

$$E_{exc}(N_{\rm Ni}, N_{\rm Pt}) = \frac{E_{coh}^{NP}(N_{\rm Ni}, N_{\rm Pt}) - N_{\rm Ni}\,\mu_{Ni}^{\text{bulk Ni}} - N_{\rm Pt}\,\mu_{Pt}^{\text{bulk Pt}}}{(N_{\rm Ni} + N_{\rm Pt})^{\frac{2}{3}}} \tag{1}$$

In the previous equation, $E_{coh}^{NP}(N_{\rm Ni}, N_{\rm Pt}) = E_{tot}^{NP}(N_{\rm Ni}, N_{\rm Pt}) - N_{\rm Ni}\,E_{\rm Ni}^{at} - N_{\rm Pt}\,E_{\rm Pt}^{at}$ where $E_{\rm i}^{at}$ ($i \in$ Pt,Ni) are the energies of isolated atoms and $E_{tot}^{NP}(N_{\rm Ni}, N_{\rm Pt})$ is the total energy of the nanoparticle. $\mu_{Ni}^{\text{bulk Ni}}$ and $\mu_{Pt}^{\text{bulk Pt}}$ correspond to the chemical potentials of Ni and Pt elements in their respective bulks. For monometallic systems, the chemical potential and

the cohesion energy are identical, for a similar sign convention.

The total cohesion energy ($E_{coh}^{NP}(N_{\mathrm{Ni}}, N_{\mathrm{Pt}})$) can also be normalized by the total number of atoms leading to a second descriptor of stability where isolated atoms are used as references:

$$E_{coh}^{NP}(N_{\mathrm{Ni}}, N_{\mathrm{Pt}}) = \frac{E_{tot}^{NP}(N_{\mathrm{Ni}}, N_{\mathrm{Pt}}) - N_{\mathrm{Ni}}\, E_{\mathrm{Ni}}^{at} - N_{\mathrm{Pt}}\, E_{\mathrm{Pt}}^{at}}{N_{\mathrm{Ni}} + N_{\mathrm{Pt}}} \tag{2}$$

A third interesting descriptor is the nanoparticle surface energy which can be measured experimentally for pure metallic nanoparticles and nanoalloys.[61,63,64] In our study we define this nanoparticle surface energy ($\gamma(N_{\mathrm{Ni}}, N_{\mathrm{Pt}})$) as the difference between the total cohesion energy of the nanocluster ($E_{coh}^{NP}(N_{\mathrm{Ni}}, N_{\mathrm{Pt}})$) and the chemical potentials of Pt (μ_{Pt}) and Ni (μ_{Ni}) elements in the various $\mathrm{Pt}_x\mathrm{Ni}_{1-x}$ alloy bulks ($L1_2$ $\mathrm{Pt_3Ni}$, $L1_0$ PtNi, $L1_2$ $\mathrm{PtNi_3}$) and also in the pure Ni and Pt bulks (for $x = 0$ and $x = 1$, respectively), by using the Gibbs phase rule (see[74] for more details). This excess energy is normalized to the nanoparticle surface area $\mathcal{A}$ which is also determined approximately (see the Supporting Information for more details and Ref.[61]):

$$\gamma(N_{\mathrm{Ni}}, N_{\mathrm{Pt}}) = \frac{E_{coh}^{NP}(N_{\mathrm{Ni}}, N_{\mathrm{Pt}}) - N_{\mathrm{Ni}}\, \mu_{\mathrm{Ni}}^{\text{bulk } \mathrm{Pt}_x\mathrm{Ni}_{1-x}} - N_{\mathrm{Pt}}\, \mu_{\mathrm{Pt}}^{\text{bulk } \mathrm{Pt}_x\mathrm{Ni}_{1-x}}}{\mathcal{A}} \tag{3}$$

Note that the strain due to the change of structure in the core of the cluster with respect to that of the FCC bulk or to the metallic coordination change at the surface is included in the calculation of the excess energy.[75]

A fourth and new descriptor of stability, named vibrational band center (VBC), is introduced in this work for the exploration of the pure Pt, Ni and alloyed PtNi nanoparticles. This descriptor uses harmonic vibrations of the nanocluster, of which the number of degrees of freedom is exact and known. The vibrations ν_i are related to the chemical bondings and the chosen normalization (number of degrees of freedom, DOF) is defined without any approximation, in contrast with two of the previous descriptors (excess energy and surface energy).

$$VBC = \frac{\Sigma_i^{DOF} \nu_i}{DOF} \quad (4)$$

where $DOF = 3(N_{Pt} + N_{Ni}) - 6$. This fourth descriptor is of different nature than that of the three other ones, since no total electronic energy is used in its formula. This captures the average depth of the corresponding minimum of the potential energy surface by considering its curvature from second derivatives and corresponds to the average bonding strength of all the metal-metal chemical bonds in the nanoparticle.

Among the four considered descriptors, three of them are positive values and are expressed in the following units: $E_{exc}(N_{\mathrm{Ni}}, N_{\mathrm{Pt}})$ in eV/at$^{2/3}$, $\gamma(N_{\mathrm{Ni}}, N_{\mathrm{Pt}})$ in J.m^{-2}, VBC in meV/DOF. For the excess and surface energies, the lower the positive value, the more stable the nanoparticle, whereas, for the vibrational band center, the meaning is opposite. For the excess and surface energies, the stability ordering can cover the complete range of chemical composition in the nanoalloys. On the contrary, for the vibrational band center, a strict comparison of stability can be carried out only for nanoclusters of identical chemical composition but different morphology or arrangement (due to the mass dependence of the vibrations). The fourth descriptor $E_{coh}^{NP}(N_{\mathrm{Ni}}, N_{\mathrm{Pt}})$ is expressed in eV/at and is essentially negative: the stronger the total binding energy between atoms, the larger the stabilization of the cluster.

Results and discussion

The exploration of monometallic Pt, Ni nanoparticles and PtNi nanoalloys has been comprehensive in the range 146-201 atoms, where 8 different morphologies have been considered as depicted in Figure 1 for optimized Pt nanoparticles (see Figures S3, S5-S19 of the SI, for optimized structures of monometallic Ni and bimetallic PtNi nanoparticles in the same range of sizes). In our selection, high symmetry clusters either convex (pristine) or concave (defective) have been considered on the basis of the three classical symmetries: Mackay icosahedral Ih, decahedral $D5h$, octahedral Oh. In the icosahedral (ico) family, one magic number

147ico can be found in the range 146-201 atoms (see Figure 1(a)). Concerning the octahedral family, three different magic numbers and related morphologies are included in our set: 147cubo, 147sito and 201rto, which are illustrative of cuboctahedral (cubo), strongly irregular truncated octahedral (sito) and regular truncated octahedral (rto) clusters (see Figure 1(b), (c) and (d), respectively). Regarding the decahedral family, four different magic numbers have been chosen in our set : 181deca, 147ino, 146marks, 192marks, which illustrate the classical convex decahedral (deca), the convex ino-decahedral (ino) and the defective Marks-decahedral (marks) clusters (see Figure 1(e), (f), (g) and (h), respectively). Regarding the chemical composition and ordering of PtNi nanoalloy models, we have decided to generate families of clusters on the basis of the well-known Pt_3Ni and $PtNi_3$ $L1_2$ bulk alloys. For the octahedral family and specifically for 147cubo and 201rto clusters, it has been then possible to generate 8 crystalline particles, in the range of composition x=0.18-0.82 (x being the Pt content in the nanoalloy), as illustrated in Figure 2(a) for one example of a crystalline 201rto cluster and in Figures S5-S6, S8-S9 of the Supporting Information for all the other optimized structures. For the third cluster of the octahedral family (147sito), crystalline clusters have not been considered. The second and largest family explored in this study concerns the non-crystalline clusters; those which do not respect the $L1_2$ structure of the PtNi bulks. In this second family composed of 89 nanoclusters in the ranges 146-201 atoms and 0.07-0.93 for chemical composition, we have generated non-crystalline octahedral 147cubo, 147sito and 201rto clusters with four different subsets depending on the chemical ordering: core-shell (cf. Figure 2 (b-c) as examples), multishell (cf. Figure 2 (e-f) as examples), skin-heart (cf. Figure 2(d)) or any chemical arrangements (see Figures S5-S9 for all the optimized structures). In our heuristic approach, core-shell nanoclusters are composed of one external monolayer of pure metal A and several layers in the core of pure metal B (the role of Pt and Ni can be reversed as shown in Figures 2(b-c)). Multishell nanoclusters are composed of an alternate sequence of monometallic layers of metal A or B, from the core to the outer shell, thus meaning that two layers of equivalent metal are never in contact (the

role of Pt and Ni can be reversed as shown in Figures 2(e-f)). Skin-heart nanoclusters are introduced in this study as a generalization of core-shell clusters with a core of several layers that can be composed of various alloys (AB_2, A_2B, AB_3, A_3B, AB_4, A_4B) and an external monolayer which is pure of metal A or B. Other non-crystalline nanoclusters belonging to none of the three previous subsets are called any nanoclusters and are composed of a core of several layers that can be composed of various alloys (AB_3 or A_3B) and a monolayer outer shell that can be composed of various alloys also (AB_2, AB_3, AB_4, A_3B, A_4B, A_8B, A_9B). In the family of non-crystalline nanoclusters, we have generated as expected a large number of icosahedral 147ico, ino-decahedral 147ino, decahedral 181deca, Marks-decahedral 146marks and 192marks, by exploring the four subsets of chemical arrangements presented before (see Figures S10-S19 for all the optimized structures). Note in passing that amorphous nanoclusters have not been considered as starting morphologies in our geometry optimizations. However, for nanoclusters rich in Ni in the outer shell, and at the opposite rich in Pt in the core, the DFT calculations show that the optimal structures lose their high initial symmetry corresponding to Oh, Ih and $D5h$. In the optimized structures, the outer shell can be amorphous, melt or dislocated, while the core can stay either rather symmetric or partially amorphous (see Figures S5-S19 of the SI for examples).

Beyond the range of size 146-201 atoms, where we have explored more than one hundred nanoclusters, the set has been extended to larger nanoparticles in the range 309-976 atoms, with three typical sizes around the magic numbers 309, 561 and 923 atoms (see Figure 3 for optimized Ni nanoparticles and Figure S4 of the SI for equivalent optimized Pt nanoclusters). For these larger clusters, both monometallic and nanoalloys have been optimized by DFT calculations with the following list of classical symmetries. For the icosahedral family, the magic numbers 309ico, 561ico and 923ico have been selected as depicted in Figure 3(a-c). For the octahedral family, the chosen numbers have been 314ito, 586rto and 976ito, thus including regular and irregular truncated octahedra as shown in Figure 3(d-f). For the Marks-decahedral family, the three retained magic numbers have been 318marks, 585marks,

967marks (cf. Figure 3(g-i)). Those symmetries and families of magic numbers have been retained in this selection due to their competitiveness at smaller size in the range 146-201 atoms, as it will be discussed later on. For the large nanoalloy clusters, only a selection of two specific chemical arrangements (core-shell and multishell presenting Pt-skin terminations in the surface) for the icosahedral family has been considered, as illustrated in Figure 4. The justification of this choice will come later on when energetics will be analyzed comparatively between all the classical symmetries. In Figure 4, the optimized structures of the PtNi nanoalloys 147ico, 309ico, 561ico and 923ico have been reported, for (a,c,e,g) core-shell Pt-skin and (b,d,f,h) multishell Pt-skin, respectively (see also complementary Figures S20-S22 for all the optimized structures of 309ico, 314ito and 318marks families).

The first energetic analysis based on the calculation of excess energy normalized to $N^{2/3}$ is exposed in Figure 5(a) for monometallic Pt and Ni nanoparticles in the range 13-976 atoms. Below 146 atoms, six additional magic numbers have been considered in the list of clusters (icosahedral 13ico, regular truncated octahedral 38rto, Marks-decahedral 49marks, icosahedral 55ico, Marks-decahedral 75marks, irregular truncated octahedral 79ito, as illustrated in Figures S1-S2 of the Supporting Information). For pure Pt and Ni nanoclusters, the six families (*FCC* Pt, ico Pt, Marks Pt, *FCC* Ni, ico Ni and Marks Ni) follow an expected trend against the approximate number of surface atoms ($N^{2/3}$), with a local minimum in the range 146-314 atoms for Pt and 147-201 atoms for Ni (see Table 1 for complementary results, especially at size 147 atoms with cuboctahedral and ino-decahedral morphologies, but also Table S4 for all the results in the range 13-976 atoms). Regarding pure Pt nanoclusters, the *FCC* and Marks-decahedral forms are competitive in stability below 79 atoms, then the Marks-decahedral form becomes the most stable one for 146 atoms, and finally *FCC* nanoparticles are the mot stable clusters in the range 201-976 atoms. Note in passing that the icosahedral forms are never competitive for pure Pt clusters (Pt13ico being not represented in Figure 5(a) due to its high excess energy of 5.08 eV, see Table S4 of the SI). Concerning pure Ni nanoclusters, the icosahedral morphology is the most stable one in the range 13-561 atoms,

with a competition with *FCC* and Marks clusters at small size (below 49 atoms). There is an inversion of stability between icosahedral and *FCC* clusters in the range 561-923 atoms, since Ni976ito cluster is more stable than Ni923ico (Ni967marks being the least stable form at this size).

This first analysis related to pure Pt and Ni nanoclusters in the range 13-976 atoms is globally consistent with previous conclusions based on quenched molecular dynamics simulations, using two different semiempirical many-body potentials (RGL and EAM parametrized by Voter), of Pt and Ni nanoclusters up to sizes N = 40000 atoms.[41,42] Our DFT results are also compatible with those obtained by a very recent SCGA-NNP study for Pt nanoparticles below 3 nm.[40] From a qualitative standpoint, the crossover between icosahedral and octahedral forms for Ni nanoparticles is predicted similarly from both approaches, DFT and semiempirical potentials. For Pt nanoparticles, the icosahedral shape is never competitive whatever the method, whereas both decahedral and octahedral forms are the most stable ones. However, from a quantitative standpoint, the crossover sizes change significantly between *ab initio* and semi-empirical approaches. According to our analysis, the crossover between forms occurs at lower sizes, especially for the DFT modeling of Ni nanoparticles. Our DFT results are thus in better agreement with other theoretical studies based on ECT/QAM approaches and alternative effective potential.[43–45] For Ni nanoparticles, only one study based on a SCGA-NNP approach has reported on a crossing between isosahedral and truncated octahedral forms at an even lower size of 1.75 nm.[40] For the icosahedral clusters, the Rosette-like surface reconstruction is stabilizing for Pt55ico, Pt147ico and Pt309ico, and largely unfavorable for Ni147ico and Ni309ico, as illustrated in the literature.[76,77] However the corresponding energy gain of about -1.5 meV.at^{-1} in the case of Pt will not change the global picture regarding the non-competitiveness of the icosahedral symmetry. Another option aiming to increase the stability of the icosahedral Pt and Ni nanoparticles is the presence of a single central metallic vacancy, as suggested in the literature for Cu, Ag and Au.[78] A systematic comparison of defective Pt and Ni icosahedral nanoclusters exhibiting

such a central vacancy with plain corresponding systems has been addressed in Table S9 and Figure S26 of the Supporting Information. According to our predictions, defective Pt icosahedral nanoclusters are systematically more stable than their equivalent plain nanoparticles whatever the chosen stability descriptor. However, the corresponding energetic gain is not enough to change the global picture, which remains in favor of the truncated octahedral morphology, by far more competitive than the icosahedral symmetry. In contrast, for the Ni nanoparticles, the presence of a central vacancy does not improve the stability of the icosahedral morphology.

The stability of PtNi nanoalloys expressed by the nanoparticle excess energy normalized to the approximate number of surface atoms (see Eq. 1) has been explored intensively in the range 146-201 atoms as exposed in Figure 6, by considering the following magic numbers and related symmetries: 146marks, 147cubo, 147ino, 147ico, 181deca, 192marks and 201rto (See Tables S5-S7 of the SI for more details). Regarding the chemical composition, crystalline and non-crystalline nanoalloys have been modeled, as illustrated in Figure 2, by focusing the search in the range of composition x=0.6-0.75. From a general standpoint, the convex hull of the most stable PtNi nanoclusters along the chemical composition resembles a catenary mathematical function, indicative of an exothermic mixing energy, classically observed for miscible metals such as Pt and Ni (see Figure 6(a) and (b)). Due to the large miscibility of these two metals, a minimum value of the convex hull is observed at the composition x=0.5 (maximal mixing energy for $L1_0$ PtNi). However, due to the small sizes of the considered nanoclusters in the range 146-201 atoms and to our choice of exploring more precisely compositions in the range 0.6-0.75, the minimum is shifted toward richer compositions in Pt. In the range 146-201 atoms, the most stable systems are icosahedral $Pt_{104}Ni_{43}$ (x=0.707) and $Pt_{92}Ni_{55}$ (x=0.626) nanoclusters belonging to the family of 147ico magic number, according to this stability descriptor (see the two marked red hollow circles in Figure 6(a)). Regarding chemical ordering, both nanoalloys correspond to multishell and core-shell arrangement with a Pt-skin, respectively (see Figures S10-S11 of the Supporting Information). Two additional

nanoclusters belonging to the *FCC* and Marks-decahedral families (201rto and 192marks, respectively) are found to be metastable just above the two icosahedral most competitive nanoparticles: $Pt_{140}Ni_{61}$ for 201rto (x=0.697) and $Pt_{134}Ni_{58}$ for 192marks (x=0.698) (as marked in Figure 6(a)) with a dark blue hollow square for 201rto, and a dark green full triangle for 192marks). The corresponding chemical ordering is a multishell arrangement with a Pt-skin for both nanoclusters (see Figures S8-S9 and S18-S19).

From a more general standpoint, the envelope of the most stable nanoalloys over the complete range of compositions shows a narrow competition between icosahedral (147ico), Marks-decahedral (192marks), truncated octahedral (201rto and 147sito), regular decahedral and ino-decahedral (181deca and 147ino) forms, with a clear preference for two magic numbers and symmetries: 147ico and 201rto (cf. Figure 6(a)). Regarding the chemical ordering along the envelope of the most competitive nanoparticles (see Figure 6(b)), no clear preference is registered. Concerning now the less competitive symmetries, 147cubo nanoalloys provide less stable clusters in the *FCC* family, as well as 146marks, 147ino and 181deca forms in the decahedral family. Regarding the chemical ordering, it should be noted that the Ni-skin nanoclusters appearing in the composition range 0.25-0.40 in Figure 6(b) are not favorable from a stability point of view, with an excess energy above 4.5 eV. This suggests that a more specific global optimization study would help to demonstrate the benefit of segregating a fraction of Pt atoms toward the surface of these nanoalloys to improve their stability.

In light of the two most competitive nanoclusters obtained in the composition range 0.6-0.75 targeted in this study (147ico with Pt-skin core-shell and multishell chemical arrangements, see Figure 6), the relative stability ordering has been explored at larger size, in the range 309-923 atoms for PtNi icosahedral nanoparticles, as depicted in Figure 4 for the optimized structures, Figures 5(b) and (c) for the corresponding excess energies and Figures 6(a) and (b) for the comparison with other nanoclusters (see also Table S8 for more details and Figures S20-S21 for optimized structures of PtNi nanoalloys in the range 309-318

atoms). According to our DFT study, when the size of the PtNi icosahedral nanocluster increases from 147 to 923 atoms, the corresponding excess energy diminishes from 3.28 to 2.87 eV for multishell chemical ordering, whereas it ranges from 3.31 to 3.21 eV for core-shell ordering with a local minimum at 3.21 eV corresponding to the $Pt_{252}Ni_{309}$ cluster ($x = 0.449$). Whatever the size of the icosahedral PtNi nanoparticle and its composition, the multishell ordering is systematically favored compared to core-shell arrangement. The most stable nanoparticle is the icosahedral $Pt_{567}Ni_{356}$ ($x = 0.614$) system with a multishell ordering which ends up at the surface with a Pt-skin and a corresponding excess energy of 2.87 eV.

In summary, for PtNi bimetallic nanoparticles, our DFT results based on excess energy calculations thus conclude on the preference of icosahedral structures for nanoclusters in the range 146-201 atoms with very competitive metastable octahedral forms. The multishell and core-shell orderings are clearly favored with a slight preference for multishell nanoclusters at the size of 147 atoms. By increasing the size of the cluster from 147 to 923 atoms, the multishell ordering becomes much more stable than the core-shell one. Regarding the morphological competition between symmetries, our results can be directly compared to those exposed recently in a SCGA-NNP investigation in the range 140-4033 atoms.[40] Most of their results predicted below 3 nm are compatible with those provided by our DFT study, when the analysis is restricted to the stability order predicted by the excess energy normalized to $N^{2/3}$. Below 3 nm, we also observe a preference for Ih symmetry over the range of composition 0.5-0.7, whereas for chemical composition over 0.7, the truncated octahedral clusters (Oh) are found more stable. Regarding now the chemical ordering, our DFT results showing a preference for multishell arrangement with Pt-skin agree with all the previous classical approaches based on effective potentials and global optimization methods, which had concluded also on a multishell arrangement with an almost complete Pt-skin outer-shell and a Ni-enrichment in the first subsurface layer of octahedral nanoclusters.[4,46,51] Recent SCGA-NNP results showing a preferential Pt-skin chemical ordering at the surface and a

favored multishell ordering with Ni in the first sub-layer for icosahedral PtNi nanoparticles[40] are thus consistent with our DFT analysis. This agreement on the chemical ordering is also extended to the truncated octahedral nanoclusters (Oh), for which a more stable skin-heart chemical ordering, presenting a regular alloy in the core of the NP is observed. A fair agreement between our DFT analysis and the previous SCGA-NNP approach concerns the mixing energy of PtNi nanoalloys, of which the definition is recalled in Eq. S1 of the Supporting Information. As presented in Figures S24 and S25 in the Supporting Information, the largest exothermic gain is observed for an icoashedral PtNi cluster of 147 atoms with a mixing energy of -0.200 eV.at^{-1} for a chemical composition of 0.707. Such value is larger than the one predicted for the Pt_3Ni bulk (-0.057 eV.at^{-1} or -1.307 kcal.mol^{-1}.at^{-1}), which is in good agreement with measurements (-0.064 eV.at^{-1} or -1.46 kcal.mol^{-1}.at^{-1}), as recalled in Table S2 of the Supporting Information. When the size of the icosahedral cluster increases from 147 ato 923 atoms, the mixing energy tends to decrease in absolute value for reaching -0.157 eV.at^{-1}. Our predictions with the PBE dDsC functional are consistent with previous SCGA-NNP results at a quantitative standpoint.[40]

An alternative interesting analysis concerns the calculations of the nanoparticle surface energy plotted against the chemical composition. In fact, recent measurements of nanoparticle surface energy for liquid Au, Cu and AuCu nanoalloys have introduced a Vegard's rulelike dependence close to linearity.[64] By applying Eq. 3 to evaluate the nanoparticle surface energy for all the optimized monometallic Pt, Ni and bimetallic PtNi nanoclusters in the range 147-201 atoms, a similar graphic has been plotted and exposed in Figure 7. In this figure, for each particular magic number and related morphology (147ico, 147cubo, 147ino, 181deca, 192marks and 201rto), the predicted nanoparticle surface energies have been plotted against chemical composition x. For PtNi nanoalloys, only the structures presenting the lowest values of surface energy for a given value of x have been reported on the graphic, thus meaning that only the most stable chemical orderings have been presented in the figure (see Figure S23 of the SI for a more complete graphic exposing all the computed values). Concerning the

predicted values of surface energies for the considered nanoclusters, a direct comparison with measurements is not possible to date due to the lack of available measurements. However, DFT calculations of surface energies related to extended Pt and Ni surfaces can be compared to available measurements and previous theoretical predictions as detailed in Table S3 of the SI. For Pt nanoparticles in the range 146-318 atoms, our average predicted value over all the competitive morphologies and symmetries is 1.55 J.m^{-2}, whereas for Ni nanoclusters our average value is 2.02 J.m^{-2} in an equivalent size range, at the PBE-dDsC level. These computed average values are smaller than our predicted values for extended surfaces or other corresponding theoretical works[57,58] and than experimental measurements for polycrystalline solids (2.20-2.49 J.m^{-2} for Pt[79–81] and 2.08-2.45 J.m^{-2} for Ni[79–81]), probably due to the small size of the considered nanoclusters. Regarding now the evolution of nanoparticle surface energy as a function of the chemical composition, the computed values are oscillating around an average linear trend for each magic number and associated morphology, as depicted in Figure 7. The slopes and offsets of these linear correlations differ significantly from one symmetry to another one, although all the predicted slopes are negative in the range -0.45/-0.84 J.m^{-2}, while the offsets are varying in the range 1.56-2.48 J.m^{-2}. According to the stability ordering, the truncated octahedral family 201rto is the most stable one over the whole range of composition. Then comes the Marks-decahedral family 192marks of PtNi nanoclusters. Moreover, when one compares the three competitive families 147cubo, 147ino and 147ico, for which the number of metallic atoms is the same, the cuboctahedral and ino-decahedral sets of PtNi clusters dominate at the level of stability over the icosahedral clusters, in the whole range of composition. Hence these latter conclusions differ in average with those resulting from predictions of excess energies in favor of PtNi icosahedral nanoclusters, except for compositions close to 0.7. These discrepancies concerning the morphological competition of PtNi nanoparticles on the basis of two different descriptors, excess energy and surface energy, which differ only from the normalization, question the relevance of the choice of such a normalization.

In order to go further in the comparative analysis of the predictions offered by each stability descriptor, a complete set of computed values is reported on Table 1 for monometallic Pt, Ni and bimetallic PtNi nanoparticles in the range 147-201 atoms. All the key high symmetries are represented and for PtNi nanoalloys, only a set of clusters exhibiting very similar compositions close to 0.7 has been selected to ease the comparison. Indeed, since the chemical composition does not very significantly around 0.7, the computed vibrational band centers can be compared between nanoalloys. The four descriptors defined in Eqs.1-4 have been calculated at the same level of accuracy and exchange-correlation functional. For Pt nanoparticles, the picture is clear-cut. The four descriptors strictly agree, first on the most stable nanoparticle (truncated octahedral Pt201rto) in the corresponding range of sizes, and second on the most stable nanocluster at the specific size of 147 atoms (strongly irregular truncated octahedral Pt147sito), where four morphologies are competing (147ico, 147ino, 147cubo and 147sito). In the case of Ni nanoclusters, the comparison is less conclusive since the descriptors offer different predictions. Concerning the most stable nanoparticle in the whole range of size, three descriptors (cohesion energy, surface energy and vibrational band center) predict that the truncated octahedral Ni201rto is the most stable cluster, whereas the excess energy supports a clear preference for the icosahedral Ni147ico system. At the specific size of 147 atoms, two descriptors of different nature (surface energy and vibrational band center) are in favor of the strongly irregular truncated octahedral Ni147sito. In contrast, the two other descriptors (cohesion energy and excess energy) predict that the icosahedral Ni147ico nanocluster is the most stable one. Such discrepancies are also seen for the comparative analysis of the PtNi nanoalloys in the range 147-201 atoms. As in the case of monometallic Ni nanoclusters, three descriptors (cohesion energy, surface energy and vibrational band center) agree on the most stable nanoparticle in the whole range of sizes (truncated octahedral $Pt_{141}Ni_{60}$rto); the excess energy alternatively predicting a more favored icosahedral $Pt_{104}Ni_{43}$ico nanocluster. At the size of 147 atoms, two descriptors (cohesion energy and excess energy) agree on the preferential stability of an icosahedral $Pt_{104}Ni_{43}$ico

nanoparticle, whereas the two other ones (surface energy and vibrational band center) are in favor of octahedral nanoclusters (strongly irregular truncated octahedral $Pt_{105}Ni_{42}$sito and cuboctahedral $Pt_{104}Ni_{43}$cubo, respectively). As a final remark, our theoretical study based on DFT calculations performed in accurate computational conditions demonstrate the high difficulty to be conclusive about the absolute stability of Ni and PtNi nanoparticles in a narrow range of sizes and chemical compositions when no experimental reference can be directly used to quantitatively validate the theoretical predictions. This work illustrates the high importance of convincing experimentalists to investigate nanoparticle energetics, in particular surface energy as previously proposed for other metals such as Ag, Au, Cu nanoparticles and AuCu nanoalloys.[63,64]

Conclusion

In the present study, the structural, energetic, chemical ordering and magnetic properties of a large set of sizes and morphologies have been explored for monometallic Pt, Ni and bimetallic PtNi nanoparticles, on the basis of accurate density functional theory calculations considering spin polarization and van der Waals interactions. Several stability descriptors have been considered in idealistic conditions of temperature and pressure, from historical descriptors based on computed DFT total electronic energy to a new descriptor which uses the second derivatives of the potential energy surface (vibrations or chemical bonding strength). A detailed and comparative analysis of the theoretical predictions has been proposed in the range 147-201 atoms for the pure Pt, Ni nanoparticles and PtNi nanoalloys. While for Pt nanoclusters, the four stability descriptors unanimously predict a preference for the truncated octahedral morphology, they disagree regarding the most stable morphology of Ni and PtNi nanoparticles. The excess energy normalized to the approximate number of surface atoms would support the Mackay icosahedral structure for Ni and for PtNi nanoclusters, with core-shell and multishell chemical ordering, whereas the three other descriptors rather conclude

on a preferential truncated octahedral form with a skin-heart arrangement for PtNi nanoalloys. The observed discrepancies set the question of the impact of the normalization in the predictive power of those stability descriptors, especially in the case of a narrow range of sizes and a small change in the number of atoms. While excess energy and nanoparticle surface energy systematically suffer from an approximate normalization (number of surface atoms and nanoparticle surface area, respectively), the cohesion energy normalized by the total number of atoms is also approximate in its normalization when nanoalloys are at stake (different metals being considered equivalently in the average). The fourth and new descriptor proposed in this study, named vibrational band center, does not suffer from this issue, since its normalization is always exact (number of degrees of freedom). However, for nanoalloys its applicability is restricted to narrow ranges of chemical compositions, due to the different masses of metals. In summary, this investigation demonstrates the importance of validating these theoretical descriptors from a quantitative standpoint with measurements. On that level, nanoparticle surface energy and vibrational band center, which are observables, open such a possibility, and invite experimentalists to examine the corresponding properties for Pt, Ni and PtNi nanoparticles.

Acknowledgement

The authors thank Dr Rodrigo Ferreira de Morais, University of Uberlandia, Brazil, for his initial contribution related to spin-polarized GGA-PBE calculations of PtNi nanoalloys in the range 38-201 atoms (FCC clusters) and related scientific discussions. His interesting results have not been reported here since van der Waals interactions had not been considered in his developments. They thank Dr Mathilde Iachella for scientific discussions related to her PhD results on AuCu nanoalloys in the range 38-201 atoms (FCC clusters). The authors thank GENCI for the access on national HPC resources of IDRIS and TGCC in Paris, and of CINES in Montpellier (projects 609 and 99642). They also thank mesocenters PSMN in Lyon

and EXPLOR hosted by the Université de Lorraine (project 2017M4XXX0108), for CPU time and assistance. The authors thank the CPER/SYSPROD 2015-2022 project (N°2019-AURA-P5B) and AXELERA Pôle de Compétitivité (PSMN Data Center). This work is supported by the European Integrated Center for the Development of New Metallic Alloys and Compounds. Emily Gaudry acknowledges financial support through the COMETE project (COnception in silico de Matériaux pour l'EnvironnemenT et l'Énergie) co-funded by the European Union under the program FEDER-FSE Lorraine et Massif des Vosges 2014-2020.

Supporting Information Available

Complementary DFT results related to monometallic Pt, Ni bulk, surfaces and nanoparticles, and to bimetallic PtNi bulk and nanoalloys.

- Table S1. Structural, energetic and magnetic properties of monometallic Pt and Ni bulks (various functionals).
- Table S2. Structural, energetic and magnetic properties of PtNi alloy bulks (various functionals).
- Table S3. Structural, energetic and magnetic properties of monometallic Pt and Ni extended flat surfaces (various functionals).
- Table S4. Structural, energetic and magnetic properties of monometallic Pt and Ni nanoclusters in the range 13-976 atoms at the PBE-dDsC level.
- Table S5. Structural, composition, chemical ordering, energetic and magnetic properties of PtNi nanoalloys (147cubo, 147sito and 201rto families at the PBE-dDsC level).
- Table S6. Structural, composition, chemical ordering, energetic and magnetic properties of PtNi nanoalloys (147ico, 147ino and 181deca families at the PBE-dDsC level).

- Table S7. Structural, composition, chemical ordering, energetic and magnetic properties of PtNi nanoalloys (146marks and 192marks families at the PBE-dDsC level).

- Table S8. Structural, composition, chemical ordering, energetic and magnetic properties of PtNi nanoalloys (309ico, 314ito, 318marks, 561ico and 923ico families at the PBE-dDsC level).

- Table S9. Comparative analysis of structural, energetic and magnetic properties for monometallic Mackay icosahedral and defective icosahedral Pt and Ni nanoclusters in the range 54-309 atoms at the PBE-dDsC level.

- Figure S1. Optimized structures of Pt nanoparticles in the range 13-79 atoms at the PBE-dDsC level.

- Figure S2. Optimized structures of Ni nanoparticles in the range 13-79 atoms at the PBE-dDsC level.

- Figure S3. Optimized structures of Ni nanoparticles in the range 146-201 atoms at the PBE-dDsC level.

- Figure S4. Optimized structures of Pt nanoparticles in the range 309-976 atoms at the PBE-dDsC level.

- Figure S5-S6. Optimized structures of cuboctahedral (cubo) Pt_xNi_y ($x + y = 147$ atoms) nanoalloys at the PBE-dDsC level.

- Figure S7. Optimized structures of strongly irregular truncated octahedral (sito) Pt_xNi_y ($x + y = 147$ atoms) nanoalloys at the PBE-dDsC level.

- Figure S8-S9. Optimized structures of regular truncated octahedral (rto) Pt_xNi_y ($x + y = 201$ atoms) nanoalloys at the PBE-dDsC level.

- Figure S10-S11. Optimized structures of Mackay icosahedral (ico) Pt_xNi_y ($x+y = 147$ atoms) nanoalloys at the PBE-dDsC level.

- Figure S12-S13. Optimized structures of ino-decahedral (ino) Pt_xNi_y ($x + y = 147$ atoms) nanoalloys at the PBE-dDsC level.

- Figure S14-S15. Optimized structures of regular decahedral (deca) Pt_xNi_y ($x+y = 181$ atoms) nanoalloys at the PBE-dDsC level.

- Figure S16-S17. Optimized structures of Marks-decahedral (marks) Pt_xNi_y ($x+y = 146$ atoms) nanoalloys at the PBE-dDsC level.

- Figure S18-S19. Optimized structures of Marks-decahedral (marks) Pt_xNi_y ($x+y = 192$ atoms) nanoalloys at the PBE-dDsC level.

- Figure S20. Optimized structures of Mackay icosahedral (ico) Pt_xNi_y ($x + y = 309$ atoms) nanoalloys at the PBE-dDsC level.

- Figure S21. Optimized structures of irregular truncated octahedral (ito) Pt_xNi_y ($x + y = 314$ atoms) nanoalloys at the PBE-dDsC level.

- Figure S22. Optimized structures of Marks-decahedral (marks) Pt_xNi_y ($x + y = 318$ atoms) nanoalloys at the PBE-dDsC level.

- Figure S23. Nanoparticle surface energy γ against the chemical composition for monometallic Pt and Ni and bimetallic PtNi nanoparticles, in the range 146-923 atoms.

- Figures S24-S25. Convex hulls of mixing energy against the chemical composition for bimetallic PtNi nanoparticles, in the range 146-923 atoms.

- Figure S26. Optimized structures of monometallic defective icosahedral Pt and Ni nanoparticles in the range 54-308 atoms.

- Equation S1. Definition of the mixing energy in binary nanoalloys normalized to the total number of metallic atoms.

Figure 1: Selected morphologies of monometallic Pt, Ni and bimetallic PtNi nanoparticles in the range 146-201 atoms: illustrations with optimized structures of (a) Mackay icosahedron Pt147ico (Ih symmetry, $\varnothing = 1.55$ nm), (b) cuboctahedron Pt147cubo (Oh symmetry, $\varnothing = 1.61$ nm), (c) strongly irregular truncated octahedron Pt147sito ($C1$ symmetry, $\varnothing = 1.63$ nm), (d) regular truncated octahedron Pt201rto (Oh symmetry, $\varnothing = 1.69$ nm), (e) regular decahedron Pt181deca ($D5h$ symmetry, $\varnothing = 1.71$ nm), (f) regular ino-decahedron Pt147ino ($D5h$ symmetry, $\varnothing = 1.61$ nm), (g) Marks-decahedron Pt146marks ($D5h$ symmetry, $\varnothing = 1.42$ nm) and (h) Marks-decahedron Pt192marks ($D5h$ symmetry, $\varnothing = 1.57$ nm). Pt atoms are depicted in gray, vertices with balls, the chemical bonds belonging to edges and facets with joint sticks, core atoms with solid representation.

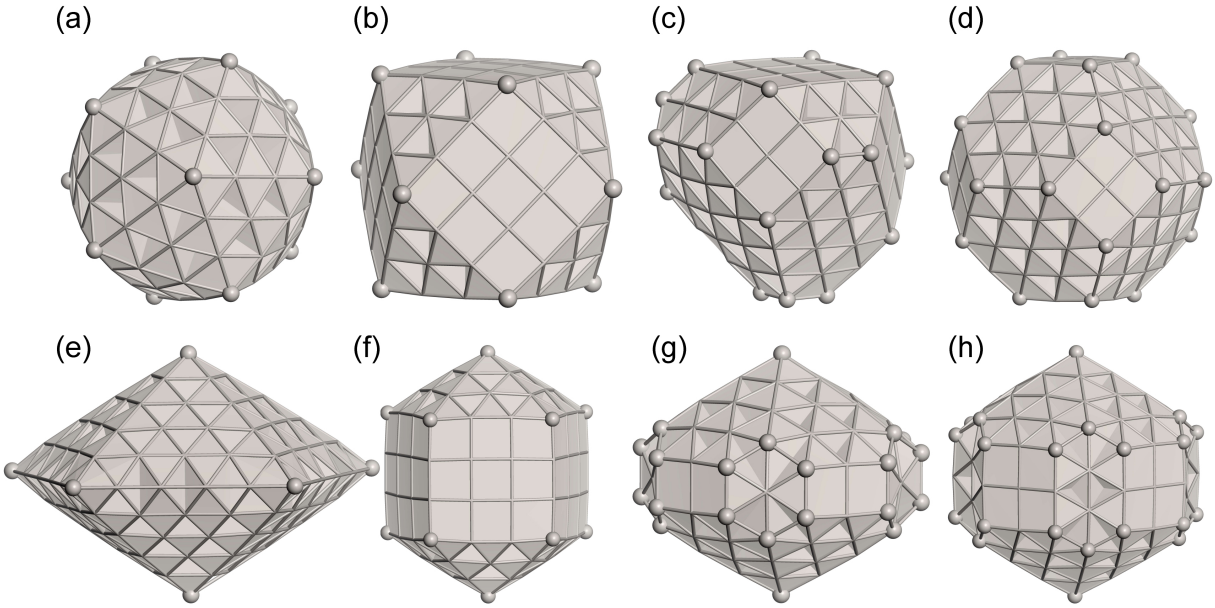

Figure 2: Families of chemical ordering in PtNi nanoalloys in the case of 201rto nanoclusters: (a) crystalline $Pt_{57}Ni_{144}$ (1 example) versus (b-f) non-crystalline nanoalloys (5 examples); (b-c) core-shell $Pt_{122}Ni_{79}$ and $Pt_{79}Ni_{122}$ (Pt-skin and Ni-skin, respectively), (d) skin-heart $Pt_{141}Ni_{60}$ (1 example); (e-f) multishell $Pt_{140}Ni_{61}$ and $Pt_{61}Ni_{140}$ (Pt-skin and Ni-skin, respectively). Pt atoms are depicted in gray, Ni in blue. To show the chemical ordering inside the clusters, a slice has been systematically canceled laterally. Surface and interior atoms (visible after being stripped) are drawn with balls while core atoms with solid representation.

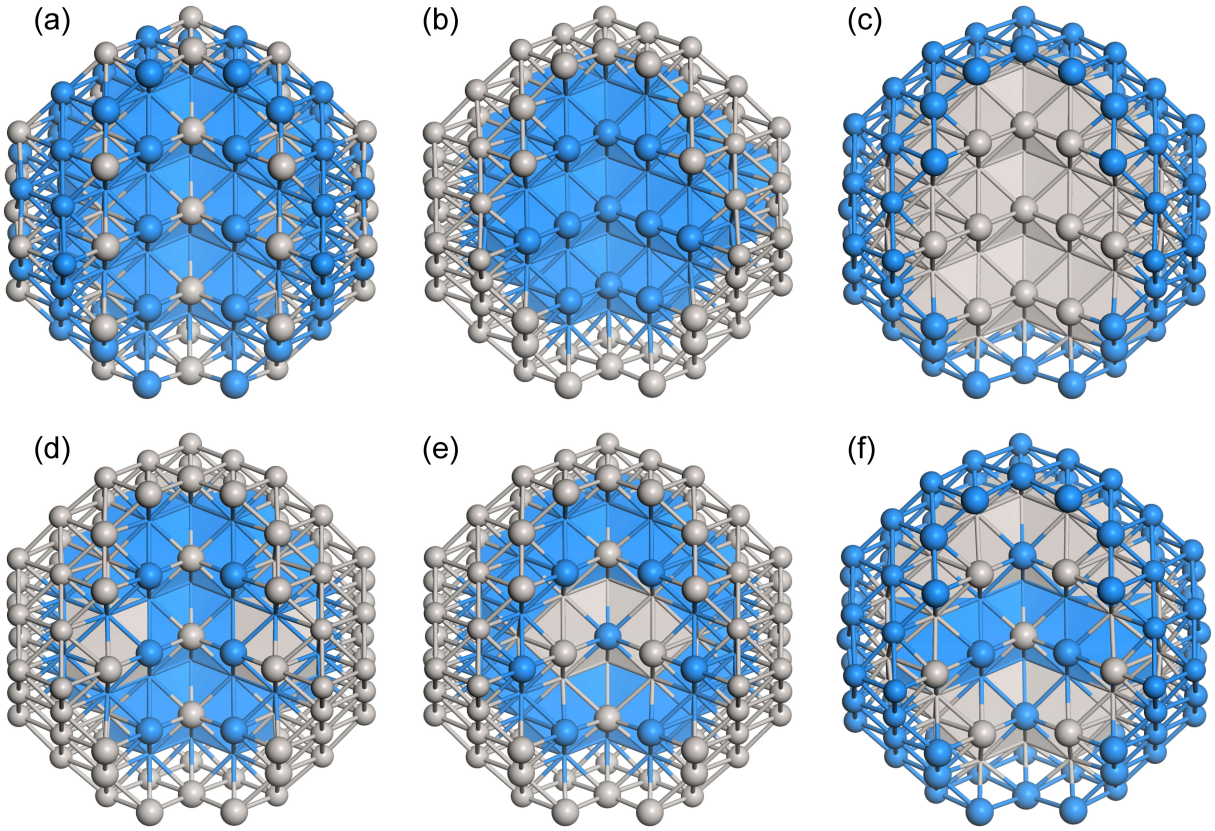

Table 1: Comparative analysis of relative stability order for monometallic Pt, Ni and bimetallic PtNi nanoparticles, in the range 147-201 atoms. Key morphologies and symmetries are considered (Mackay icosahedral 147ico, Ih, FCC cuboctahedral 147cubo, strongly irregular truncated octahedral 147sito, regular truncated octahedral 201rto, Oh, and ino-decahedral 147ino, Marks-decahedral 192marks, $D5h$). For PtNi nanoalloys, the chemical ordering is indicated in each case as well as the chemical composition x. The total spin polarization $\vec{M}$ (μ_B) is addressed for all the nanoclusters. Cohesion energy normalized to total number of metallic atoms E_{coh} (eV/at), excess energy E_{exc} normalized to approximate number of surface atoms $N^{2/3}$ (eV/at$^{2/3}$), nanoparticle surface energy γ (J.m^{-2}) and vibrational band center (meV/DOF) are indicated for all the nanoparticles.

Cluster	Structure	Ordering	x	$\vec{M}$	E_{coh}	E_{exc}	γ	VBC
Ni147	Mackay ico	-	0	96.6	-4.401	**4.206**	2.204	11.75
Ni147	ino-deca	-	0	97.5	-4.357	4.441	2.252	11.70
Ni192	Marks-deca	-	0	137.5	-4.460	4.259	1.978	11.97
Ni147	cubo	-	0	98.1	-4.350	4.475	2.261	11.83
Ni147	sito	-	0	100.7	-4.376	4.338	1.723	12.02
Ni201	rto	-	0	138.1	**-4.476**	4.232	**1.649**	**12.09**
Pt141Ni60	rto	skin-heart	0.701	78.7	**-5.068**	3.439	**1.148**	**8.59**
Pt135Ni57	Marks-deca	skin-heart	0.703	68.9	-5.044	3.531	1.408	8.45
Pt104Ni43	Mackay ico	multishell	0.707	66.2	-5.038	**3.280**	1.540	8.38
Pt104Ni43	ino-deca	multishell	0.707	61.2	-4.983	3.570	1.548	8.48
Pt104Ni43	cubo	multishell	0.707	56.7	-4.963	3.672	1.568	8.51
Pt104Ni43	cubo	skin-heart	0.707	54.0	-4.950	3.746	1.598	8.53
Pt105Ni42	Mackay ico	skin-heart	0.714	58.2	-4.997	3.516	1.642	8.34
Pt105Ni42	ino-deca	skin-heart	0.714	45.1	-4.933	3.853	1.662	8.35
Pt105Ni42	sito	multishell	0.714	54.6	-4.958	3.586	1.202	8.37
Pt147	Mackay ico	-	1	0	-5.017	4.393	1.819	6.71
Pt147	ino-deca	-	1	0	-5.011	4.428	1.782	6.86
Pt192	Marks-deca	-	1	0	-5.129	4.157	1.542	6.94
Pt147	cubo	-	1	0	-5.003	4.471	1.787	6.84
Pt147	sito	-	1	0	-5.048	4.231	1.341	6.98
Pt201	rto	-	1	0	**-5.152**	**4.085**	**1.273**	**7.03**

Figure 3: Optimized structures of large Ni nanoparticles in the range 309-976 atoms: (a) Mackay icosahedron Ni309ico (Ih symmetry, $\varnothing = 1.86$ nm), (b) Mackay icosahedron Ni561ico (Ih symmetry, $\varnothing = 2.33$ nm), (c) Mackay icosahedron Ni923ico (Ih symmetry, $\varnothing = 2.81$ nm), (d) irregular truncated octahedron Ni314ito (Oh symmetry, $\varnothing = 1.84$ nm), (e) regular truncated octahedron Ni586rto (Oh symmetry, $\varnothing = 2.29$ nm), (f) irregular truncated octahedron Ni976ito (Oh symmetry, $\varnothing = 2.77$ nm), (g) Marks decahedron Ni318marks ($D5h$ symmetry, $\varnothing = 1.74$ nm), (h) Marks decahedron Ni585marks ($D5h$ symmetry, $\varnothing = 2.19$ nm), (i) Marks decahedron Ni967marks ($D5h$ symmetry, $\varnothing = 2.63$ nm). Ni atoms are depicted in blue, vertices with balls, the chemical bonds belonging to edges and facets with joint sticks, core atoms with solid representation.

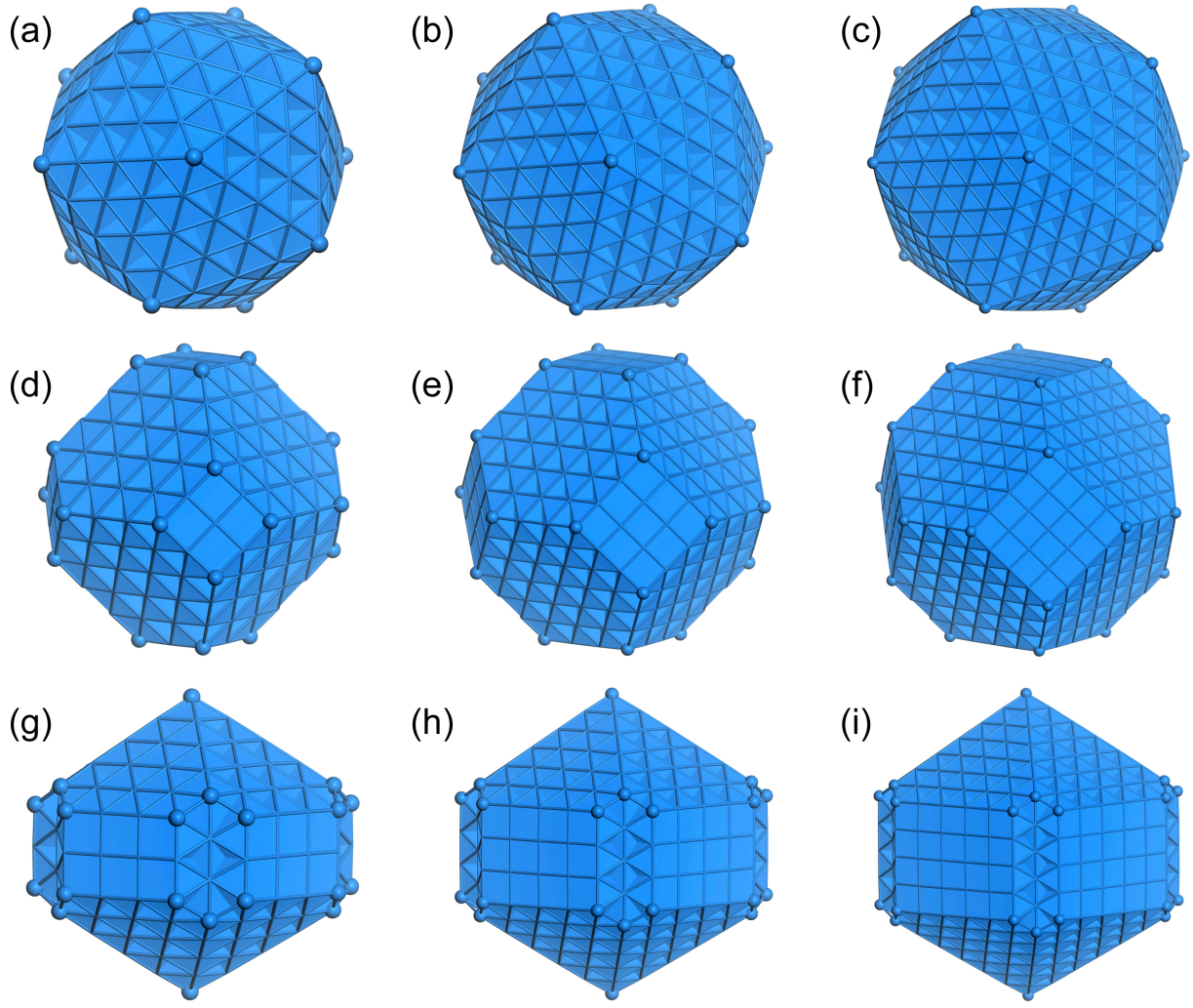

Figure 4: Optimized structures of PtNi Mackay icosahedral nanoparticles (Ih symmetry) in the range 147-923 atoms and with Pt-skin terminations: (a) core-shell $Pt_{92}Ni_{55}$ ($\varnothing$ = 1.49 nm), (b) multishell $Pt_{104}Ni_{43}$ ($\varnothing$ = 1.51 nm), (c) core-shell $Pt_{162}Ni_{147}$ ($\varnothing$ = 2.0 nm), (d) multishell $Pt_{205}Ni_{104}$ ($\varnothing$ = 2.02 nm), (e) core-shell $Pt_{252}Ni_{309}$ ($\varnothing$ = 2.50 nm), (f) multishell $Pt_{356}Ni_{205}$ ($\varnothing$ = 2.54 nm), (g) core-shell $Pt_{362}Ni_{561}$ ($\varnothing$ = 3.00 nm), (h) multishell $Pt_{567}Ni_{356}$ ($\varnothing$ = 3.05 nm). Pt atoms are depicted in gray, Ni in blue. To show the chemical ordering inside the clusters, a slice has been systematically canceled laterally. Surface and interior atoms (visible after being stripped) are drawn with balls while core atoms with solid representation.

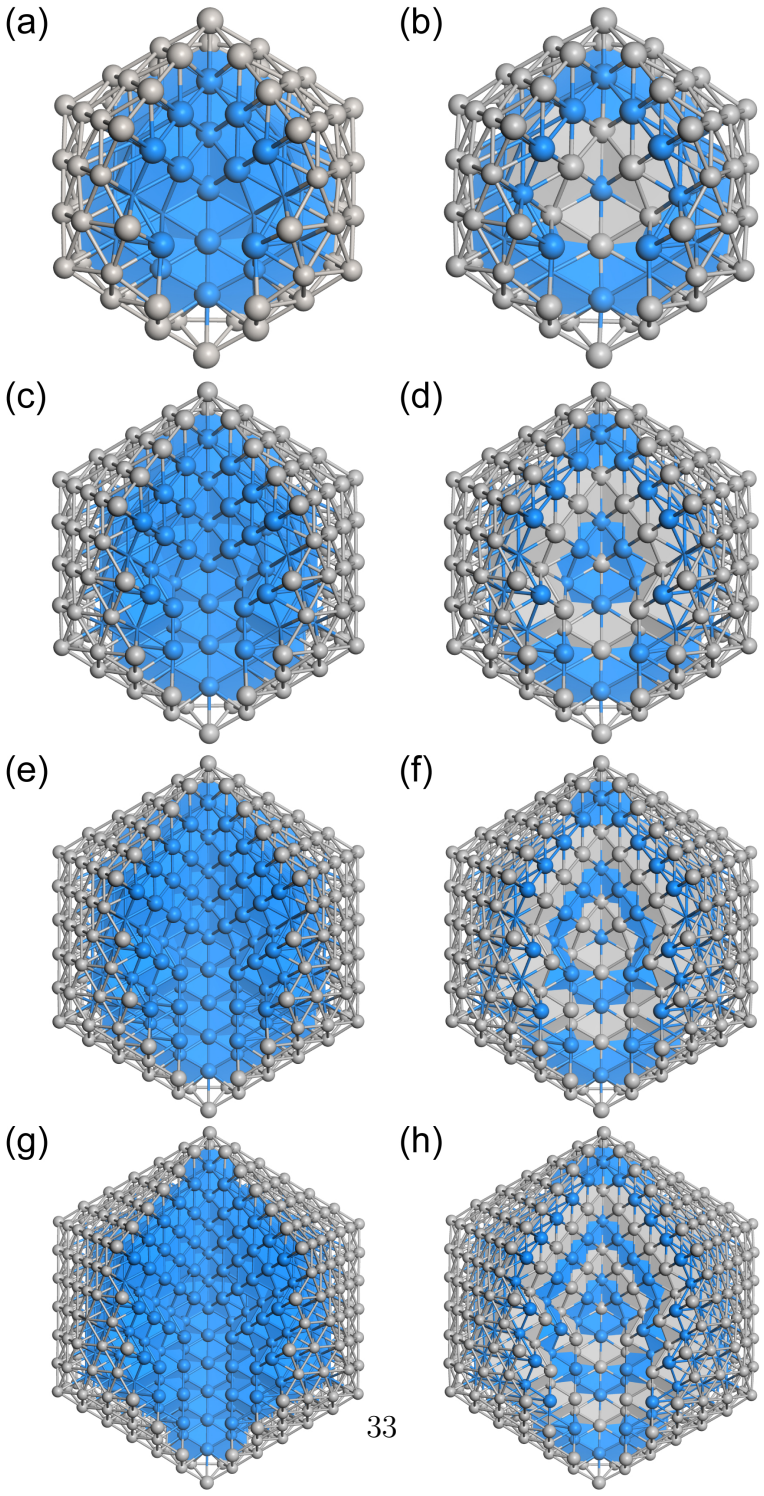

Figure 5: Excess energy E_{exc} (eV/at$^{2/3}$) normalized to approximate number of surface atoms N$^{2/3}$ (a) against the number of atoms for monometallic Pt (blue) and Ni (red) nanoparticles in the range 13-976 atoms (three families in competition: Marks-decahedral, *FCC* and Mackay icosahedral nanoclusters; *FCC* set being composed of regular and irregular truncated octahedral clusters, and one strongly irregular truncated octahedral 147sito nanoparticle); (b) against the total number of Pt and Ni atoms for PtNi nanoalloys in the range 147-923 atoms, only for Mackay icosahedral shape and Pt-skin termination (core-shell, in orange, versus multishell, in green, chemical orderings); (c) against the chemical composition for the same family of clusters of (b). (see Figures S1-S2 in the Supporting Information for the optimized monometallic Pt and Ni clusters in the range 13-79 atoms, Figure 1 and Figure S3 for optimized Pt and Ni clusters in the range 146-201 atoms, respectively, Figure 3 and Figure S4 for optimized Ni and Pt clusters in the range 309-976 atoms, respectively. See also Table S4 for all the energetic data).

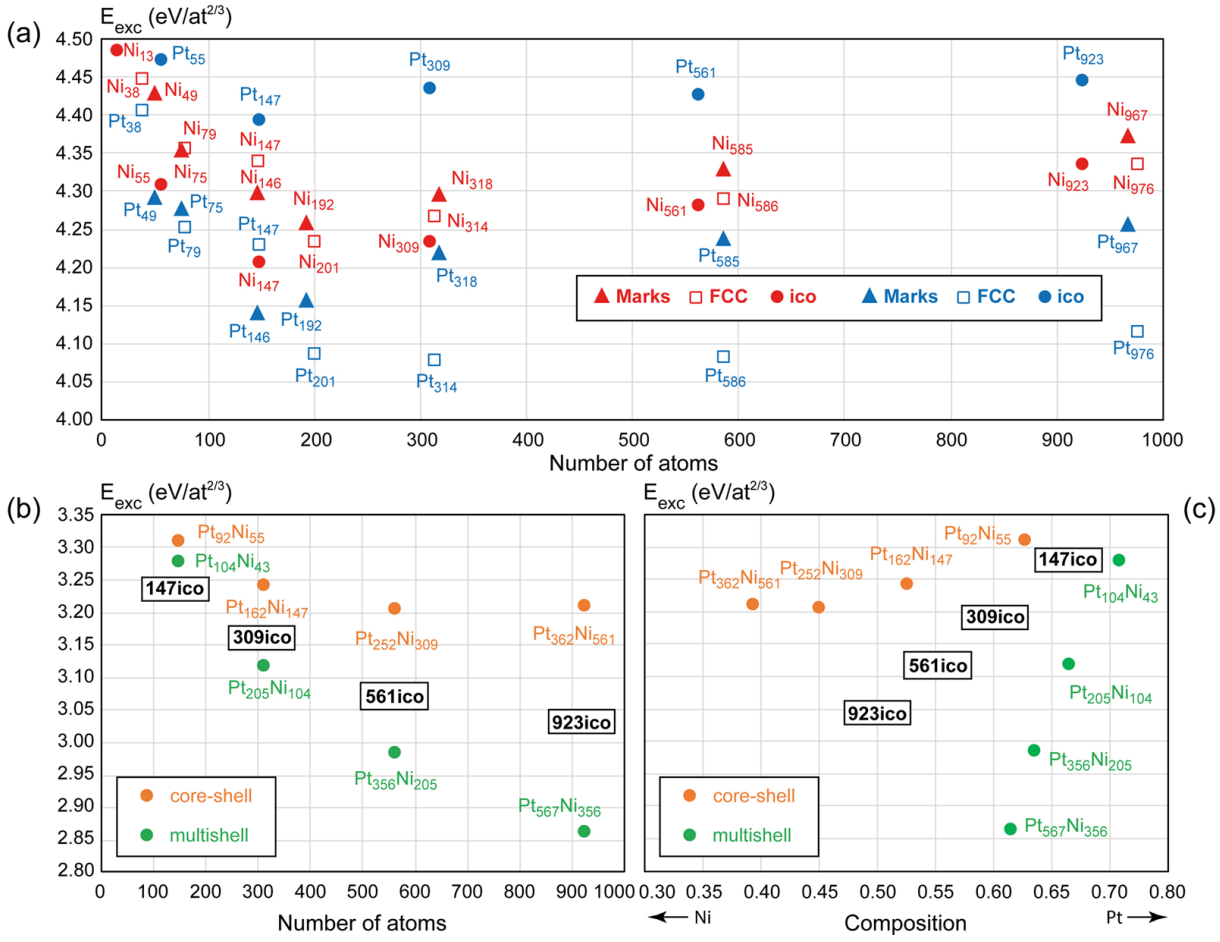

Figure 6: Convex hull of excess energy E_{exc} (eV/at$^{2/3}$) normalized to approximate number of surface atoms N$^{2/3}$ against the chemical composition for monometallic Pt and Ni and bimetallic PtNi nanoparticles, in the range 146-923 atoms. The markers and related colors define in (a) the different sets of magic numbers and related morphologies and in (b) the different chemical orderings and crystallinities. The most competitive nanoclusters are indicated in both graphics.

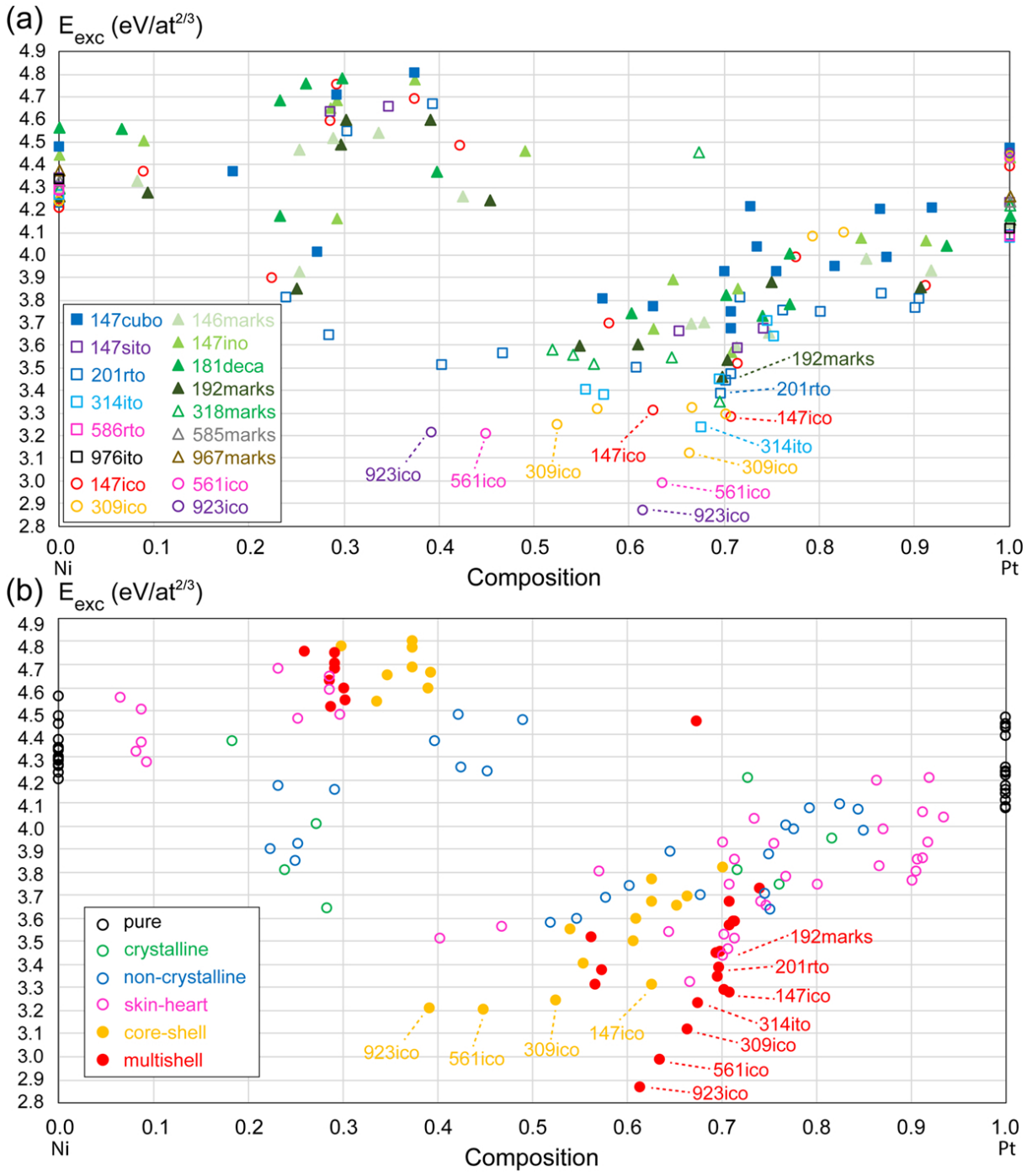

Figure 7: Nanoparticle surface energy γ (J.m^{-2}) against the chemical composition for monometallic Pt and Ni and bimetallic PtNi nanoparticles, in the range 147-201 atoms. The markers and related colors define the different sets of magic numbers and related morphologies. Only most competitive nanoalloys for a given composition are reported on the graphic. For each magic number and associated morphology, the parameters of linear regressions are presented with slopes $\Delta\gamma$, offsets γ_0 (both in J.m^{-2}) and regression coefficients R^2.

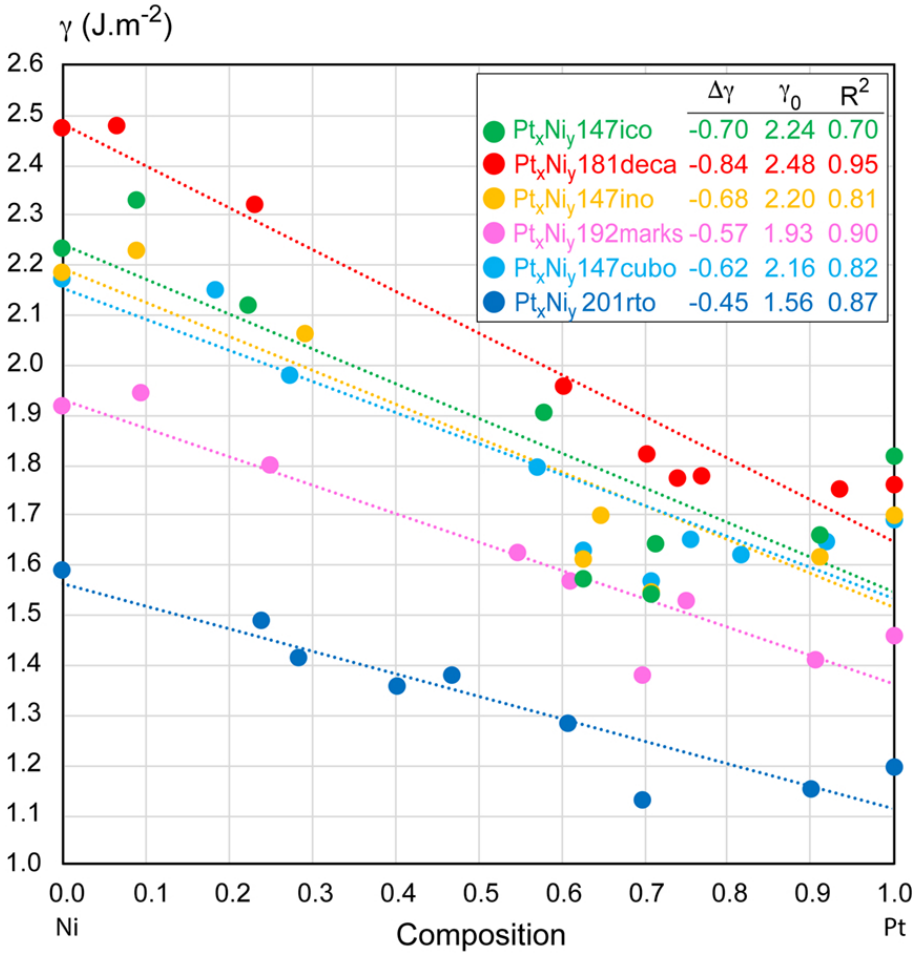

References

(1) Stamenković, V.; Schmidt, T. J.; Ross, P. N.; Marković, N. M. Surface Composition Effects in Electrocatalysis: Kinetics of Oxygen Reduction on Well-Defined Pt_3Ni and Pt_3Co Alloy Surfaces. *The Journal of Physical Chemistry B* **2002**, *106*, 11970–11979.

(2) Stamenković, V.; Schmidt, T.; Ross, P.; Marković, N. Surface segregation effects in electrocatalysis: kinetics of oxygen reduction reaction on polycrystalline Pt_3Ni alloy surfaces. *Journal of Electroanalytical Chemistry* **2003**, *554-555*, 191–199, Special issue in memory of Professor M.J. Weaver.

(3) Debe, M. K. Electrocatalyst Approaches and Challenges for Automotive Fuel Cells. *Nature* **2012**, *486*, 43.

(4) Fowler, B.; Lucas, C. A.; Omer, A.; Wang, G.; Stamenković, V. R.; Marković, N. M. Segregation and stability at $Pt_3Ni(111)$ surfaces and $Pt_{75}Ni_{25}$ nanoparticles. *Electrochimica Acta* **2008**, *53*, 6076–6080.

(5) Stamenkovic, V. R.; Fowler, B.; Mun, B. S.; Wang, G.; Ross, P. N.; Lucas, C. A.; Marković, N. M. Improved Oxygen Reduction Activity on $Pt_3Ni(111)$ via Increased Surface Site Availability. *Science* **2007**, *315*, 493–497.

(6) Wang, C.; Markovic, N. M.; Stamenkovic, V. R. Advanced Platinum Alloy Electrocatalysts for the Oxygen Reduction Reaction. *ACS Catalysis* **2012**, *2*, 891–898.

(7) Stamenkovic, V. R.; Mun, B. S.; Mayrhofer, K. J. J.; Ross, P. N.; Markovic, N. M. Effect of Surface Composition on Electronic Structure, Stability, and Electrocatalytic Properties of Pt-Transition Metal Alloys: Pt-Skin versus Pt-Skeleton Surfaces. *Journal of the American Chemical Society* **2006**, *128*, 8813–8819.

(8) Greer, J. R. Nanoframe Catalysts. *Science* **2014**, *343*, 1319–1320.

(9) Chen, C.; Kang, Y.; Huo, Z.; Zhu, Z.; Huang, W.; Xin, H. L.; Snyder, J. D.; Li, D.; Herron, J. A.; Mavrikakis, M. et al. Highly Crystalline Multimetallic Nanoframes with Three-Dimensional Electrocatalytic Surfaces. *Science* **2014**, *343*, 1339–1343.

(10) Becknell, N.; Kang, Y.; Chen, C.; Resasco, J.; Kornienko, N.; Guo, J.; Markovic, N. M.; Somorjai, G. A.; Stamenkovic, V. R.; Yang, P. Atomic Structure of Pt_3Ni Nanoframe Electrocatalysts by in Situ X-ray Absorption Spectroscopy. *Journal of the American Chemical Society* **2015**, *137*, 15817–15824.

(11) Becknell, N.; Son, Y.; Kim, D.; Li, D.; Yu, Y.; Niu, Z.; Lei, T.; Sneed, B. T.; More, K. L.; Markovic, N. M. et al. Control of Architecture in Rhombic Dodecahedral Pt–Ni Nanoframe Electrocatalysts. *Journal of the American Chemical Society* **2017**, *139*, 11678–11681.

(12) Chen, S.; Niu, Z.; Xie, C.; Gao, M.; Lai, M.; Li, M.; Yang, P. Effects of Catalyst Processing on the Activity and Stability of Pt–Ni Nanoframe Electrocatalysts. *ACS Nano* **2018**, *12*, 8697–8705.

(13) Dubau, L.; Nelayah, J.; Moldovan, S.; Ersen, O.; Bordet, P.; Drnec, J.; Asset, T.; Chattot, R.; Maillard, F. Defects do Catalysis: CO Monolayer Oxidation and Oxygen Reduction Reaction on Hollow PtNi/C Nanoparticles. *ACS Catalysis* **2016**, *6*, 4673–4684.

(14) Leteba, G. M.; Wang, Y.-C.; Slater, T. J. A.; Cai, R.; Byrne, C.; Race, C. P.; Mitchell, D. R. G.; Levecque, P. B. J.; Young, N. P.; Holmes, S. M. et al. Oleylamine Aging of PtNi Nanoparticles Giving Enhanced Functionality for the Oxygen Reduction Reaction. *Nano Letters* **2021**, *21*, 3989–3996.

(15) Kwon, H.; Kabiraz, M. K.; Park, J.; Oh, A.; Baik, H.; Choi, S.-I.; Lee, K. Dendrite-Embedded Platinum–Nickel Multiframes as Highly Active and Durable Electrocatalyst toward the Oxygen Reduction Reaction. *Nano Letters* **2018**, *18*, 2930–2936.

(16) Chen, J.; Lim, B.; Lee, E. P.; Xia, Y. Shape-controlled synthesis of platinum nanocrystals for catalytic and electrocatalytic applications. *Nano Today* **2009**, *4*, 81–95.

(17) Chang, Q.; Xu, Y.; Duan, Z.; Xiao, F.; Fu, F.; Hong, Y.; Kim, J.; Choi, S.-I.; Su, D.; Shao, M. Structural Evolution of Sub-10 nm Octahedral Platinum–Nickel Bimetallic Nanocrystals. *Nano Letters* **2017**, *17*, 3926–3931.

(18) Leteba, G. M.; Mitchell, D. R. G.; Levecque, P. B. J.; Macheli, L.; van Steen, E.; Lang, C. I. High-Index Core–Shell Ni–Pt Nanoparticles as Oxygen Reduction Electrocatalysts. *ACS Applied Nano Materials* **2020**, *3*, 5718–5731.

(19) Shokhen, V.; Zysler, M.; Shviro, M.; Zitoun, D.; Chatenet, M. Carbon-Supported PtNi Nanocrystals for Alkaline Oxygen Reduction and Evolution Reactions: Electrochemical Activity and Durability upon Accelerated Stress Tests. *ACS Applied Energy Materials* **2020**, *3*, 8858–8870.

(20) Alia, S. M.; Ngo, C.; Shulda, S.; Ha, M.-A.; Dameron, A. A.; Weker, J. N.; Neyerlin, K. C.; Kocha, S. S.; Pylypenko, S.; Pivovar, B. S. Exceptional Oxygen Reduction Reaction Activity and Durability of Platinum–Nickel Nanowires through Synthesis and Post-Treatment Optimization. *ACS Omega* **2017**, *2*, 1408–1418.

(21) Wang, Q.; Tian, H.; Yu, Y.; Li, J.; Rao, P.; Li, R.; Du, Y.; Jia, C.; Luo, J.; Deng, P. et al. Synthesis and Design of a Highly Stable Platinum Nickel Electrocatalyst for the Oxygen Reduction Reaction. *ACS Applied Materials & Interfaces* **2021**, *13*, 52681–52687.

(22) Li, M.; Zhao, Z.; Cheng, T.; Fortunelli, A.; Chen, C.-Y.; Yu, R.; Zhang, Q.; Gu, L.; Merinov, B. V.; Lin, Z. et al. Ultrafine jagged platinum nanowires enable ultrahigh mass activity for the oxygen reduction reaction. *Science* **2016**, *354*, 1414–1419.

(23) Song, X.; Luo, S.; Fan, X.; Tang, M.; Zhao, X.; Chen, W.; Yang, Q.; Quan, Z. Controlled

Synthesis of PtNi Hexapods for Enhanced Oxygen Reduction Reaction. *Frontiers in Chemistry* **2018**, *6*, 468.

(24) Feng, Q.; Wang, X.; Klingenhof, M.; Heggen, M.; Strasser, P. Low-Pt NiNC-Supported PtNi Nanoalloy Oxygen Reduction Reaction Electrocatalysts—In Situ Tracking of the Atomic Alloying Process. *Angewandte Chemie International Edition* **2022**, *61*, e202203728.

(25) Li, S.; Yan, X.; Shi, M.; Wei, P.; Lu, H.; Zhang, Z.; Zhang, Y.; Li, Y. Electrodeposition of Pt-Ni nanoparticles on graphene as an electrocatalyst for oxygen reduction reaction. *Frontiers in Chemistry* **2022**, *10*, 1061838.

(26) Duc Le, T.; Ahemad, M. J.; Kim, D.-S.; Lee, B.-H.; Oh, G.-J.; Shin, G.-S.; Nagappagari, L. R.; Dao, V.; Van Tran, T.; Yu, Y.-T. Synergistic effect of Pt-Ni dual single-atoms and alloy nanoparticles as a high-efficiency electrocatalyst to minimize Pt utilization at cathode in polymer electrolyte membrane fuel cells. *Journal of Colloid and Interface Science* **2023**, *634*, 930–939.

(27) Huang, J.; Sementa, L.; Liu, Z.; Barcaro, G.; Feng, M.; Liu, E.; Jiao, L.; Xu, M.; Leshchev, D.; Lee, S.-J. et al. Experimental Sabatier Plot for Predictive Design of Active and Stable Pt-Alloy Oxygen Reduction Reaction Catalysts. *Nature Catalysis* **2022**, *5*, 513–523.

(28) Ferreira de Morais, R.; Franco, A. A.; Sautet, P.; Loffreda, D. Interplay between Reaction Mechanism and Hydroxyl Species for Water Formation on Pt(111). *ACS Catalysis* **2015**, *5*, 1068–1077.

(29) Ferreira de Morais, R.; Franco, A. A.; Sautet, P.; Loffreda, D. How Does the Surface Structure of Pt–Ni Alloys Control Water and Hydrogen Peroxide Formation? *ACS Catalysis* **2016**, *6*, 5641–5650.

(30) Pacchioni, G.; Chung, S.-C.; Krüger, S.; Rösch, N. On the evolution of cluster to bulk properties: a theoretical LCGTO-LDF study of free and coordinated Ni_n clusters (n=6-147). *Chemical Physics* **1994**, *184*, 125–137.

(31) Montejano-Carrizales, J. M.; Iñiguez, M. P.; Alonso, J. A.; López, M. J. Theoretical study of icosahedral Ni clusters within the embedded-atom method. *Physical Review B* **1996**, *54*, 5961–5969.

(32) Michaelian, K.; Rendón, N.; Garzón, I. L. Structure and energetics of Ni, Ag, and Au nanoclusters. *Physical Review B* **1999**, *60*, 2000–2010.

(33) Grigoryan, V. G.; Springborg, M. A theoretical study of the structure of Ni clusters (NiN). *Physical Chemistry Chemical Physics* **2001**, *3*, 5135–5139.

(34) Futschek, T.; Hafner, J.; Marsman, M. Stable structural and magnetic isomers of small transition-metal clusters from the Ni group: an ab initio density-functional study. *Journal of Physics: Condensed Matter* **2006**, *18*, 9703.

(35) Longo, R. C.; Gallego, L. J. Structures of 13-atom clusters of fcc transition metals by ab initio and semiempirical calculations. *Physical Review B* **2006**, *74*, 193409.

(36) Da Silva, J. L. F.; Kim, H. G.; Piotrowski, M. J.; Prieto, M. J.; Tremiliosi-Filho, G. Reconstruction of core and surface nanoparticles: The example of Pt_{55} and Au_{55}. *Physical Review B* **2010**, *82*, 205424.

(37) Welborn, M.; Tang, W.; Ryu, J.; Petkov, V.; Henkelman, G. A combined density functional and x-ray diffraction study of Pt nanoparticle structure. *The Journal of Chemical Physics* **2011**, *135*, 014503.

(38) Chou, J. P.; Hsing, C. R.; Wei, C. M.; Cheng, C.; Chang, C. M. Ab initio random structure search for 13-atom clusters of fcc elements. *Journal of Physics: Condensed Matter* **2013**, *25*, 125305.

(39) Isenberg, N. M.; Taylor, M. G.; Yan, Z.; Hanselman, C. L.; Mpourmpakis, G.; Gounaris, C. E. Identification of optimally stable nanocluster geometries via mathematical optimization and density-functional theory. *Molecular Systems Design & Engineering* **2020**, *5*, 232–244.

(40) Han, S.; Barcaro, G.; Fortunelli, A.; Lysgaard, S.; Vegge, T.; Hansen, H. A. Unfolding the Structural Stability of Nanoalloys via Symmetry-Constrained Genetic Algorithm and Neural Network Potential. *NPJ Computational Materials* **2022**, *8*, 121.

(41) Baletto, F.; Ferrando, R.; Fortunelli, A.; Montalenti, F.; Mottet, C. Crossover among structural motifs in transition and noble-metal clusters. *The Journal of Chemical Physics* **2002**, *116*, 3856–3863.

(42) Baletto, F.; Ferrando, R. Structural properties of nanoclusters: Energetic, thermodynamic, and kinetic effects. *Reviews of Modern Physics* **2005**, *77*, 371–423.

(43) Negreiros, F. R.; Soares, E. A.; de Carvalho, V. E. Energetics of free pure metallic nanoclusters with different motifs by equivalent crystal theory. *Physical Review B* **2007**, *76*, 205429.

(44) Barnard, A. S.; Konishi, H.; Xu, H. F. Morphology mapping of platinum catalysts over the entire nanoscale. *Catalysis Science & Technology* **2011**, *1*, 1440–1448.

(45) Cleveland, C. L.; Landman, U. The energetics and structure of nickel clusters: Size dependence. *The Journal of Chemical Physics* **1991**, *94*, 7376–7396.

(46) Wang, G.; Van Hove, M.; Ross, P.; Baskes, M. Quantitative prediction of surface segregation in bimetallic Pt–M alloy nanoparticles (M=Ni,Re,Mo). *Progress in Surface Science* **2005**, *79*, 28–45, X-th Symposium on Surface Physics, Prague, Czech Republic, 2005.

(47) Datta, A.; Duan, Z.; Wang, G. Influence of surface segregation on the elastic property of Pt–Ni alloy nanowires. *Computational Materials Science* **2012**, *55*, 81–84.

(48) Cheng, D.; Yuan, S.; Ferrando, R. Structure, chemical ordering and thermal stability of Pt–Ni alloy nanoclusters. *Journal of Physics: Condensed Matter* **2013**, *25*, 355008.

(49) Guedes-Sobrinho, D.; Nomiyama, R. K.; Chaves, A. S.; Piotrowski, M. J.; Da Silva, J. L. F. Structure, Electronic, and Magnetic Properties of Binary Pt_nTM_{55-n} (TM = Fe, Co, Ni, Cu, Zn) Nanoclusters: A Density Functional Theory Investigation. *The Journal of Physical Chemistry C* **2015**, *119*, 15669–15679.

(50) Panizon, E.; Ferrando, R. Strain-induced restructuring of the surface in core@shell nanoalloys. *Nanoscale* **2016**, *8*, 15911–15919.

(51) Shin, Y. K.; Gai, L.; Raman, S.; van Duin, A. C. T. Development of a ReaxFF Reactive Force Field for the Pt–Ni Alloy Catalyst. *The Journal of Physical Chemistry A* **2016**, *120*, 8044–8055.

(52) Yang, Y.; Yu, H.; Cai, Y.; Ferrando, R.; Cheng, D. Origin of enhanced stability and oxygen adsorption capacity of medium-sized Pt–Ni nanoclusters. *Journal of Physics: Condensed Matter* **2018**, *30*, 285503.

(53) Miedema, A. R. Surface Energies of Solid Metals. *International Journal of Materials Research* **1978**, *69*, 287–292.

(54) Miedema, A. R. Model predictions of the dissociation energies of homonuclear and heteronuclear diatomic molecules of two transition metals. *Faraday Symposia of the Chemical Society* **1980**, *14*, 136–148.

(55) Lian, L.; Su, C.; Armentrout, P. B. Collision-induced dissociation of Ni_n^+ (n=2–18) with Xe: Bond energies, geometrical structures, and dissociation pathways. *The Journal of Chemical Physics* **1992**, *96*, 7542–7554.

(56) Medasani, B.; Park, Y. H.; Vasiliev, I. Theoretical study of the surface energy, stress, and lattice contraction of silver nanoparticles. *Physical Review B* **2007**, *75*, 235436.

(57) Akbarzadeh, H.; Abroshan, H.; Parsafar, G. A. Surface free energy of platinum nanoparticles at zero pressure: A molecular dynamic study. *Solid State Communications* **2010**, *150*, 254–257.

(58) Luo, W.; Hu, W.; Su, K.; Liu, F. The calculation of surface free energy based on embedded atom method for solid nickel. *Applied Surface Science* **2013**, *265*, 375–378.

(59) Yao, Y.; Wei, Y.; Chen, S. Size effect of the surface energy density of nanoparticles. *Surface Science* **2015**, *636*, 19–24.

(60) Vollath, D.; Fischer, F. D.; Holec, D. Surface energy of nanoparticles – influence of particle size and structure. *The Beilstein Journal of Nanotechnology* **2018**, *9*, 2265–2276.

(61) Loffreda, D.; Foster, D. M.; Palmer, R. E.; Tarrat, N. Importance of Defective and Nonsymmetric Structures in Silver Nanoparticles. *The Journal of Physical Chemistry Letters* **2021**, *12*, 3705–3711.

(62) Amara, H.; Nelayah, J.; Creuze, J.; Chmielewski, A.; Alloyeau, D.; Ricolleau, C.; Legrand, B. Effect of size on the surface energy of noble metal nanoparticles from analytical and numerical approaches. *Physical Review B* **2022**, *105*, 165403.

(63) Nanda, K. K.; Maisels, A.; Kruis, F. E.; Fissan, H.; Stappert, S. Higher Surface Energy of Free Nanoparticles. *Physical Review Letters* **2003**, *91*, 106102.

(64) Chmielewski, A.; Nelayah, J.; Amara, H.; Creuze, J.; Alloyeau, D.; Wang, G.; Ricolleau, C. Direct Measurement of the Surface Energy of Bimetallic Nanoparticles: Evidence of Vegard's Rulelike Dependence. *Physical Review Letters* **2018**, *120*, 025901.

(65) Kresse, G.; Hafner, J. Ab initio molecular dynamics for liquid metals. *Physical Review B* **1993**, *47*, 558–561.

(66) Kresse, G.; Hafner, J. Ab initio molecular-dynamics simulation of the liquid-metal–amorphous-semiconductor transition in germanium. *Physical Review B* **1994**, *49*, 14251–14269.

(67) Kresse, G.; Furthmüller, J. Efficiency of ab-initio total energy calculations for metals and semiconductors using a plane-wave basis set. *Computational Materials Science* **1996**, *6*, 15–50.

(68) Kresse, G.; Furthmüller, J. Efficient iterative schemes for ab initio total-energy calculations using a plane-wave basis set. *Physical Review B* **1996**, *54*, 11169–11186.

(69) Steinmann, S. N.; Corminboeuf, C. A generalized-gradient approximation exchange hole model for dispersion coefficients. *The Journal of Chemical Physics* **2011**, *134*, 044117.

(70) Steinmann, S. N.; Corminboeuf, C. Comprehensive Benchmarking of a Density-Dependent Dispersion Correction. *Journal of Chemical Theory and Computation* **2011**, *7*, 3567–3577.

(71) Perdew, J. P.; Burke, K.; Ernzerhof, M. Generalized Gradient Approximation Made Simple. *Physical Review Letters* **1996**, *77*, 3865–3868.

(72) Kresse, G.; Joubert, D. From ultrasoft pseudopotentials to the projector augmented-wave method. *Physical Review B* **1999**, *59*, 1758–1775.

(73) He, X.; Shi, H. Size and shape effects on magnetic properties of Ni nanoparticles. *Particuology* **2012**, *10*, 497–502.

(74) Gaudry, E. *Comprehensive Inorganic Chemistry III, Theory and Bonding of Inorganic Non-molecular Systems*, Reedijk, J. and Poeppelmeier, K. R. ed.; Elsevier Ltd: Oxford,

2023; Vol. 3; Chapter An introduction to the theory of inorganic solid surfaces, pp 74–104.

(75) Nelli, D.; Roncaglia, C.; Minnai, C. Strain engineering in alloy nanoparticles. *Advances in Physics: X* **2023**, *8*, 2127330.

(76) Aprà, E.; Baletto, F.; Ferrando, R.; Fortunelli, A. Amorphization Mechanism of Icosahedral Metal Nanoclusters. *Physical Review Letters* **2004**, *93*, 065502.

(77) Nelli, D. Central vacancy creation in icosahedral nanoparticles induced by the displacement of large impurities. *European Physical Journal Applied Physics* **2022**, *97*, 18.

(78) Mottet, C.; Tréglia, G.; Legrand, B. New magic numbers in metallic clusters: an unexpected metal dependence. *Surface Science* **1997**, *383*, L719–L727.

(79) Tyson, W. R.; Miller, W. A. Surface free energies of solid metals: Estimation from liquid surface tension measurements. *Surface Science* **1977**, *62*, 267–276.

(80) Foiles, S. M.; Baskes, M. I.; Daw, M. S. Embedded-atom-method functions for the fcc metals Cu, Ag, Au, Ni, Pd, Pt, and their alloys. *Physical Review B* **1986**, *33*, 7983–7991.

(81) Skriver, H. L.; Rosengaard, N. M. Surface energy and work function of elemental metals. *Physical Review B* **1992**, *46*, 7157–7168.

TOC Graphic